Immunogenomic landscape of T cell repertoire after human lung transplantation and its clinical significance

Wenyu Jiao[1], Katherine D. Long[1], Tyla Young[1], Constanza Bay Muntnich[1], Adriana Prada Rey[1], Morcel Khwajazadah[1], Joshua H. Wang[1,2], Vineetha Mohan[1], Kortney Rogers[1], Arnold Valena[3], Joseph Costa[4], Luke Benvenuto[5], Joshua Sonett[4], Philippe Lemaitre[4], Frank D'Ovidio[4], Selim Arcasoy[5], Jianing Fu[1, *]

[1]Columbia Center for Translational Immunology, Department of Medicine, Columbia University Irving Medical Center, New York, NY, USA.

[2]Columbia College, Columbia University, New York, NY, USA.

[3]NewYork-Presbyterian Hospital, New York, United States.

[4]Department of Surgery, Columbia University Irving Medical Center, New York, NY, USA.

[5]Division of Pulmonary, Allergy, and Critical Care Medicine, Columbia University Irving Medical Center, New York, NY, USA.

*Corresponding Author:

Jianing Fu, PhD, Columbia Center for Translational Immunology,

650 West 168th Street, Black Building 1501A, New York, 10032

Email: jf2977@cumc.columbia.edu

ORCID: 0000-0003-1500-5405

Key words: lung transplantation (LuTx), immunogenomics, T cell repertoire, alloreactive T cells, microbial reactive T cells, tissue resident memory T cells, rejection, pulmonary function

Abstract (237 words)

Despite advances in surgical techniques and immunosuppression, long-term survival after lung transplantation (LuTx) remains suboptimal due to high rates of rejection, infection and graft dysfunction. To address this, we investigated post-LuTx T cell dynamics—tracking repopulation, clonal distribution, alloreactivity, and microbial reactivity—through flow cytometry and TCRβ sequencing of serial bronchoalveolar lavage (BAL) and peripheral blood samples. Pre-transplant mixed lymphocyte reactions coupled with TCRβ-seq identified alloreactive TCRs in both graft-versus-host (GvH) and host-versus-graft (HvG) directions, while pathogen-reactive clones were defined via cross-referencing with public databases. We observed progressive establishment of a recipient-derived tissue-resident memory T cell (TRM) repertoire in the BAL, stabilized predominantly by pre-existing, multi-tissue-shared TCRs. Clonal BAL–blood overlap was significantly driven by $CD8^+$ non-alloreactive recipient TCRs originating from multiple tissues. A higher HvG:GvH TCR ratio correlated with faster recipient T cell repopulation in BAL, and HvG enrichment in BAL (but not peripheral blood) was associated with early rejection and reduced pulmonary function. Pathogen-reactive TCRs expanded in BAL during infection and were enriched within the non-alloreactive repertoire. This comprehensive TCR landscape analysis highlights the dual roles of T cells in maintaining mucosal homeostasis and contributing to rejection or infection pathogenesis. These findings support the development of precise, mechanism-informed diagnostics to better tailor immunosuppression and ultimately improve LuTx outcomes. Additionally, our work establishes LuTx as a powerful model for studying human tissue-adapted immunity, offering novel insights into the establishment, maintenance, and functional specialization of TRM repertoires.

Introduction

Lung transplantation (LuTx) is the final therapeutic option for patients with end-stage respiratory diseases, including chronic obstructive pulmonary disease, idiopathic pulmonary fibrosis and pulmonary hypertension [1]. Approximately 2,500 to 3,000 LuTx procedures are performed annually in the United States in recent years, predominantly in adults (over 95%) [2]. While short-term outcomes have improved in recent years, long-term survival remains poor, with 5-year survival rate of 60% [2]. Rejection remains the primary complication limiting transplant success, even with lifelong immunosuppression [3-5]. Although most early rejection episodes can be managed by intensifying immunosuppression, these treatments increase infection risk and predispose patients to high-grade late rejections [6], both of which are key risk factors for chronic lung allograft dysfunction (CLAD), the leading cause of mortality post-LuTx [7].

A major challenge complicating clinical management after LuTx is the lack of accurate diagnostic tools for rejection. Acute cellular rejection (ACR), mediated primarily by donor-reactive recipient T cells, is histologically diagnosed by perivascular and interstitial mononuclear infiltrates in lung tissue, graded by inflammation severity in vascular (A0 to A4) and airway (B0 to B2R) compartments [8]. However, histology-based ACR diagnosis suffers from low sensitivity/ specificity, difficulties distinguishing it from infection-driven inflammation, and high interobserver variability [8-10]. Current efforts to identify novel rejection biomarkers [11-14] face a critical challenge: the inability to distinguish pathogenic donor-reactive recipient T cells from protective T-cell subsets, such as microbial-reactive recipient T cells or recipient-reactive donor T cells that combat infection or rejection, respectively. Therefore, distinguishing donor vs. recipient T cells and integrating their functional phenotypes (alloreactive vs. microbial-reactive) with clonotype tracking via TCRβ sequencing offers a promising new approach. This strategy can map T-cell origin, distribution, and participation in alloresponses and mucosal homeostasis post-LuTx,

enabling mechanistic insights into rejection and precision diagnostics to optimize immunosuppression.

Our group did extensive studies in the field of T cell immunogenomics of human alloresponses to reveal mechanisms of rejection and tolerance [15-23]. Our data in human intestinal transplantation showed that graft-versus-host (GvH) T cell clones expand in intestinal allografts and migrate into the recipient circulation and bone marrow. These GvH-reactive T cells express high levels of cytotoxic effector genes and mediate lymphohematopoietic GvH responses that attenuate host-versus-graft (HvG) T cell reactions and make space for donor hematopoietic stem and progenitor cell engraftment, promoting mixed chimerism and contributing to possible immune tolerance [15, 17, 18]. Our immune repertoire profiling of T cell clones revealed their dynamic establishment in intestinal allografts and replenishment from the circulating pool in acquiring tissue residency [23]. Like intestines, lung grafts carry large numbers of T cells and antigen-presenting cells (APCs), which may lead to bidirectional (GvH and HvG) alloresponses, the balance of which is expected to determine graft outcomes. Previous LuTx studies frequently do not distinguish donor cells from recipient cells, leading to controversies and difficulties in interpreting their clinical significance [11-13]. Even in studies demonstrated a dynamic replacement of donor T cells by the recipient T cells in lung allografts, followed by the gradual acquisition of a tissue resident memory (TRM) phenotype by graft-infiltrating recipient T cells [24, 25], critical features of donor and recipient T cells are still largely unexplored, including their clonal distribution, alloreactivity and microbial-reactivity.

To determine how functional TCR clones influence clinical outcomes after LuTx, we conducted longitudinal profiling of donor- and recipient-derived T cells in bronchoalveolar lavage (BAL),

transbronchial biopsies (TBBx), and peripheral blood samples. This approach enabled comprehensive characterization of the evolving immunogenomic landscape of T cell repertoires following LuTx at multiple levels: (1) chimeric composition, (2) phenotypic evolution, (3) pre-transplant (pre-Tx) tissue origin, and (4) alloreactive and microbial-reactive clonal dynamics. BAL-to-blood comparisons revealed how tissue-resident clones emerge over time and are associated with rejection, infection, and pulmonary dysfunction. Our study also offers a unique window into the establishment of the human TRM repertoire, uncovering evolutionary hallmarks—such as preferential persistence, phenotypic convergence, and functional compartmentalization—that inform broader principles of tissue-adapted immunity beyond the transplant context.

Result

Multilineage chimerism in blood and BAL post-Tx

A total of 13 adult LuTx recipients have been enrolled and transplanted in our cohort since November 2020 (Table S1). COVID-19 affected sample collection for several earlier enrolled patients (Pts1–6). Pts 2 and 5 were excluded from the analysis due to early death on post-operative day (POD)166 and POD16, respectively. Subsequent analysis included 11 patients: 5 female and 6 male patients aged 28 to 70 (median: 63) years at the time of transplant, who received either single LuTx, double LuTx, or liver Tx + double LuTx (Table S1). We performed flow cytometry to distinguish donor- and recipient-derived cells from T/B cell/monocyte lineages (Fig. S1A) in post-Tx peripheral blood mononuclear cell (PBMC) and BAL samples using HLA-allotype specific antibodies (Table S2) as described previously [26]. BAL is commonly used as a surrogate to monitor the immune changes in the lung allograft [24, 25]. Recipient $CD14^+$ monocytes exhibited rapid infiltration into BAL compared to recipient $CD3^+$ T cells (Fig. S1B), suggesting their potential role as APCs in priming GvH-reactive donor T cell expansion in BAL early post-Tx, consistent with our data in human intestinal transplantation [15]. A small fraction of donor T cells carried by lung graft mucosa or lymphoid tissues migrated into circulation, resulting in low levels of donor T cell chimerism in blood (<3%) (Fig. S1C). Recipient T cell reconstitution kinetics in BAL reached 50% repopulation by POD150, with notable interpatient heterogeneity (Fig. S1C). These dynamics were comprehensively evaluated for associations with bidirectional alloresponses and graft outcomes in the final Results section. B cell findings will be reported in a separate manuscript and are therefore not discussed here.

Graft-infiltrating recipient T cells gradually establish a stable repertoire with TRM phenotypes in the lung allograft, a stability primarily driven by pre-existing recipient TCRs

In line with previous report [24], we evaluated the TRM features of CD8 T cells in post-Tx BAL by flow cytometry and found that donor cells overall maintained as TRMs (Fig. 1A, 1B), while graft-infiltrating recipient cells gradually obtained TRM features by upregulating expression of CD69 and CD103 (Fig. 1A, 1B). To investigate the relationship between tissue residency and T cell clonal stability, we calculated the Jensen-Shannon Divergence (JSD) values (Fig. 1C) between TCR repertoires from BAL and PBMC samples collected at sequential post-Tx timepoints in each patient with TCRβ-seq data available (Fig. S2). Notably, JSD values in BAL significantly declined over time ($r=-0.5285$, $p=0.0046$), whereas those in PBMCs remained stable ($r=-0.3035$, $p=0.1402$). This suggests the progressive establishment of a recipient-derived TRM pool with enhanced repertoire similarity and stability in the lung allograft but not in the periphery (Fig. S2). To evaluate the impact of sampling intervals, we analyzed JSD values against ΔPOD (time between adjacent samples) and found no association with longer intervals, indicating that timing variability did not significantly bias our interpretation (Fig. S3).

To delineate mechanisms underlying post-Tx BAL repertoire stabilization, we partitioned TCRs detected in post-Tx samples into pre-existing (pre-Tx detected) donor and recipient TCRs, and "*de novo*" (post-Tx emergent) clonotypes. These were subclassified by initial detection timepoint and assessed for clonal persistence via recurrence rates of unique CDR3 sequences (Figs. 1D, S4). Pre-existing donor TCRs were not discussed further in this analysis given overall less dominant presence in post-Tx samples, although demonstrate considerable levels of clonal recurrence in post-Tx BAL (data not shown), in line with their TRM phenotypes. We observed that pre-Tx recipient TCRs detected across multiple PODs progressively accumulated in both

BAL and PBMC repertoires, with many TCR sequences identified at early point(s) recurring at later stages (PBMCs: mean 30.32% ± 18.90%; BAL: mean 17.55% ± 10.04%). In striking contrast, while newly detected post-Tx TCRs constituted a substantial proportion of both the BAL and PBMC repertoires, only a minor fraction demonstrated recurrent detection (PBMCs: mean 1.27% ± 1.38%; BAL: mean 1.77% ± 2.30%) (Figs. 1E, S4). Quantitative analysis using normalized area under curve (AUC) metrics showed pre-Tx recipient TCRs (first detected at the earliest POD) had significantly higher recurrence rates than post-Tx newly detected TCRs in both BAL and PBMC compartments (Fig. 1F). This demonstrates that repertoire stability post-Tx was primarily maintained by the pre-existing recipient TCRs rather than newly detected clones. Among pre-Tx recipient-derived TCRs, we observed that CD8 TCRs consistently demonstrated higher recurrence rates than CD4 TCRs in both BAL and PBMC compartments (Fig. S5).

Cross-tissue pre-existing recipient TCR sequences exhibited enhanced clonal recurrence in both BAL and blood compartments post-Tx

To delineate how pre-Tx recipient tissue origins (Table S3) shape post-Tx repertoire establishment, we systematically categorized recipient TCRs detected in post-Tx BAL and PBMC samples into seven groups based on their pre-Tx detection patterns: (1) lymphoid-PBMC-lung shared, (2) PBMC-lung shared, (3) lymphoid-lung shared, (4) lymphoid-PBMC shared, (5) lung only, (6) PBMC only, and (7) lymphoid only. Notably, while single-tissue-derived TCRs (groups 5–7) constituted substantial fractions of pre-Tx repertoires, their representation was markedly reduced in both post-Tx BAL and PBMCs (Figs. 2A, S6). Conversely, multi-tissue shared TCRs (groups 1–4) – particularly triple-shared clones (group 1) – dominated the post-Tx repertoires (Figs. 2A, S6).

We quantified the relative detection rates of multi-tissue shared TCRs vs. non-shared TCRs in post-Tx BAL and PBMC samples. In our representative patient analysis, shared TCR subsets, particularly lymphoid-PBMC-lung triple-shared TCRs, demonstrated significantly higher detection rates compared to non-shared TCRs (Fig. 2B). This pattern was consistent across all patients when assessed via normalized AUC analysis of detection rate kinetics in both BAL and PBMC samples, with triple-shared TCRs exhibiting the highest relative detection rates in the BAL compartment (Fig. 2C).

To quantify the temporal similarity of TCR repertoires across tissue origins, we assessed sequence overlap (templated-weighted) among non-shared, double-shared, and triple-shared TCR subsets of post-Tx BAL and PBMC samples (representative patient: Fig. 2D). Pooled analysis across all patients revealed significantly higher median overlap proportions in triple-shared vs. double-shared or non-shared subsets (Fig. 2E). While PBMC repertoires exhibited a strict hierarchical overlap pattern (triple- > double- > non-shared), BAL samples showed a similar but less pronounced trend. Collectively, our results demonstrate that TCRs detected in multiple pre-Tx recipient tissues - including peripheral blood, lung-associated lymphoid tissue, and lung parenchyma - exhibit superior engraftment potential in both BAL and blood compartments. These multi-tissue-derived TCRs showed significantly higher recurrence rates and were the primary drivers of post-Tx TCR repertoire stability.

T cell exchange between blood and BAL persists over one-year post-Tx, primarily mediated by both multi-tissue-derived recipient TCRs present prior to transplantation and recipient non-alloreactive CD8 TCRs

To elucidate the spatial dynamics of TCR repertoire distribution post-LuTx, we systematically analyzed T cell crosstalk between PBMC and BAL compartments (Fig. 3A) across three post-operative periods: early (POD<90), mid (POD90-365), and late (POD>365). Using a comparison matrix (Fig. 3B), we quantified the proportion of BAL TCR sequences detectable in corresponding PBMC samples. While no significant temporal pattern emerged in overlap fractions across periods (Fig. 3B), a persistent T cell crosstalk between peripheral blood and lung allografts was observed throughout the first year, with occasionally lower early-phase overlap (e.g., groups A, B and C in Pt9) potentially attributable to residual donor T cells in grafts. Aggregate analysis (compiled data points from groups A to I for each patient) revealed that BAL-PBMC clonal overlap was significantly enriched for recipient-derived pre-Tx TCRs (Fig. 3C), particularly triple-shared (lymphoid-PBMC-lung) TCRs (Fig. 3D) and CD8 non-alloreactive subsets (CD8 nonHvG) (Fig. 3E). These findings implicate tissue-experienced, non-alloreactive CD8 T cells act as the primary migratory population and key mediators of systemic-lung immune surveillance post-LuTx.

Microbial-reactive TCRs were enriched in lung allografts during infection and predominantly composed of non-alloreactive T cell populations

The requirement for lifelong immunosuppression in LuTx recipients significantly increases infection susceptibility. In our cohort, all patients experienced ≥1 pathogen infection, with many developing recurrent infections by diverse pathogens (Fig. 4A, Table S1). We hypothesized that non-alloreactive T cells (defined by non-reactivity to donor or recipient antigens in pre-Tx allogeneic MLRs) may persist and expand pathogen-specific clones during infection. Using a strategy we previously validated in human intestinal transplantation [23], we systematically identified microbial-reactive TCRs by cross-referencing our dataset with published TCR databases (including COVID-19-specific clones) [27-32], focusing on CDR3β (V-J-AA)

signatures. In patients with post-Tx EBV or CMV infection - the most clinically significant viral pathogens - we observed significant enrichment of EBV- or CMV-reactive TCRs in BAL and lung allografts during active infection vs. peripheral blood (Figs. 4A, 4B). These findings demonstrate that our TCR mapping approach reliably tracks pathogen-specific responses. To comprehensively characterize microbial-reactive TCRs and assess their potential alloreactive cross-reactivity, we performed detailed annotation of TCR specificity in Pt13 (as a representative case), categorizing TCR clones as alloreactive (CD4/CD8 HvG, CD4/CD8 GvH) and non-alloreactive (CD4/CD8 nonHvG, CD4/CD8 nonGvH). This analysis encompassed TCRs reactive to common bacterial/viral pathogens (Fig. 4C) and COVID-19 (Fig. S7A) in post-Tx lung, BAL, and/or PBMCs. Pooled analysis across our cohort revealed a consistent pattern: both donor- and recipient-derived non-alloreactive T cell clones demonstrated significantly greater enrichment for microbe-reactive TCRs compared to their alloreactive counterparts. This microbial-focused specialization was observed universally across all tissue compartments (lung allograft, BAL and peripheral blood), suggesting non-alloreactive clones primarily mediate pathogen surveillance (Figs. 4D, S7B).

HvG-GvH imbalance drives recipient T cell repopulation dynamics in BAL and HvG-reactive TCR enrichment in BAL correlates with early rejection and impaired pulmonary function

In line with our study in human intestinal transplantation [18], we hypothesize that the balance between GvH and HvG alloresponses may determine graft outcomes following LuTx. GvH- and HvG-reactive TCR clones were defined using pre-Tx MLRs and high-throughput TCRβ sequencing, as we previously described [15, 18]. Pre-Tx MLRs utilized donor and recipient cells isolated from lung-associated lymph nodes (LLNs). We monitored GvH- and HvG-reactive TCRs in post-Tx BAL samples from 8 patients with available pre-Tx specimens (Figs. 5A, S8A, S5).

Five patients (Pts 4/7/8/12/13) with faster recipient T cell repopulation in the BAL (Fig. S1C) showed dominant HvG- over GvH-reactive clones, which is different than the remaining 3 patients (Pts1/9/11) with slower recipient T cell repopulation in BAL (Figs. 5A, S8A). A statistically significant correlation was identified between rapid recipient T cell repopulation and a dominant ratio of HvG- to GvH-reactive TCRs in BAL (Fig. 5B), which were quantified by AUC normalized by days of measurement for both the replacement rate and HvG vs. GvH alloreactivities in the BAL. A similar trend was observed in lung transbronchial biopsies (TBBx: data not shown). Instead of looking at total TCR repertoires (Fig. 5A-B), we now focused on recipient mappable TCR repertoires (Figs. 5C-D, S8B, Table S5), defined as TCRs detectable in pre-Tx unstimulated or MLR $CFSE^{low}$ T cell populations from recipient LLNs. These repertoires include both HvG and nonHvG TCRs. During early ACR in lung allografts (Pt7 POD22, Pt9 POD68), we observed high levels of HvG TCRs among recipient mappable repertoires in BAL and, to a lesser extent, TBBx, but not in PBMCs (Fig. 5C), indicating local HvG clonal expansion correlates with early rejection. In liver allografts of Pt9, higher HvG TCR levels were seen during mild/moderate ACR (POD5) vs. minimal ACR (POD81) (Fig. 5C). In some patients, early post-Tx (within POD90) HvG peaks were identified in BAL, but not PBMCs, despite negative histopathology for ACR, but preceded late complications (e.g., late ACR [POD>200 in Pts 8, 13], *de novo* DSA [Pts 4,11,13], CLAD [Pt4], or death [Pt13 POD303, Pt4 POD1556]), suggesting undiagnosed subclinical rejection and the need for immunosuppression refinement (Figs. 5C, S8B).

To investigate the relationship between HvG responses and pulmonary function despite temporal mismatches in measurement timing, we stratified the post-Tx course into three distinct phases based on BAL HvG TCR dynamics: peak, decline and baseline (Figs. 5C, S8B, S8C). We then analyzed corresponding forced expiratory volume in one second (FEV1)

measurements (normalized to baseline values) within each phase (Fig. S8C). Strikingly, we observed a significant inverse correlation between HvG TCR levels and pulmonary function across phases. These findings establish graft-infiltrating recipient HvG-reactive T cells as potential mediators of rejection and determinants of allograft function.

Discussion

LuTx outcomes significantly lag behind those of other solid organ transplants due to at least two interrelated challenges. First, the lack of precise rejection diagnostics forces dangerous clinical trade-offs: delayed treatment leads to sustained inflammation and progressive rejection, while overimmunosuppression heightens infection risk—both accelerating CLAD, the leading cause of post-LuTx mortality. Second, donor-derived lymphocytes within the allograft play a critical role in shaping post-Tx immunity but remain poorly understood. Our study addresses this dual pathophysiology through immunogenomic profiling of both donor and recipient T cells. By temporally and spatially mapping bidirectional alloresponses (HvG and GvH) and microbial immunity, we uncover key mechanisms underlying rejection and infection. These insights directly inform novel strategies to overcome diagnostic limitations and optimize immunosuppression, ultimately bridging the LuTx outcomes gap. Our study also establishes LuTx as a powerful model for human TRM biology, providing unprecedented insight into the establishment, maintenance, and functional specialization of TRM repertoires. By overcoming the critical limitation of longitudinal access to non-lymphoid tissues—a major barrier in human immunology—we reveal conserved principles of tissue-adapted immunity with broad implications beyond transplant science.

We demonstrated the progressive establishment of a recipient-derived TRM repertoire in post-LuTx BAL, with repertoire stability predominantly driven by pre-existing, multi-tissue-shared recipient TCRs. These findings suggest a replenishment model where recipient TCRs migrate from the circulating pool, lymphoid reservoirs, or even lung parenchymal niches. This aligns with emerging evidence of re-circulating TRMs – a paradigm shift in TRM biology supported by both murine and human studies [33-38], where tissue-adapted clones retain limited migratory capacity between mucosal sites and secondary lymphoid organs. Building on our prior work in

human intestinal transplantation [23]—where single-cell RNA sequencing revealed distinct transcriptional programs in T cells shared across pre-Tx lymphoid and non-lymphoid tissues vs. tissue-restricted clones—we now establish that these multi-tissue-primed T cells tend to represent a recirculating TRM reservoir. In LuTx, such clones (particularly the lymphoid-PBMC-lung triple-shared subset) dominate graft-resident repertoires and exhibit both tissue adaptability and re-circulating potential to facilitate BAL-blood crosstalk. While recirculating TRMs exist in both CD4+ and CD8+ lineages, their dynamics are context-dependent—varying by tissue site and host environment, as demonstrated in both animal models and human studies [38-43]. Notably, we found that non-alloreactive CD8+ recipient T cells, rather than CD4+, played a more active role in BAL-blood crosstalk and were more enriched for microbial-reactive TCRs. This suggests a predominant recirculating phenotype that contributes to host defense against pathogens. Collectively, these findings refine the 'resident memory' paradigm by demonstrating that human TRMs occupy a spectrum of tissue fidelity, with multi-tissue-primed non-alloreactive CD8 T cell clones more likely to exhibit strategic circulation to surveil dispersed mucosal sites.

It is important to note that the non-alloreactive TCRs defined in our study are specific to a single donor–recipient pair within our cohort. Indeed, prior work by our colleagues has demonstrated that a very high proportion of human T cells—if not all—possess alloreactive potential against a broad array of allogeneic stimulators, as measured by MLRs [44]. Consequently, it is reasonable to infer that pathogen-reactive T cells may frequently exhibit cross-reactivity to alloantigens presented by diverse MHC combinations, consistent with previous human studies [45]. However, in the context of LuTx, where recipients are typically exposed to a single allogeneic donor (excluding re-transplantation scenarios), we observed that HvG–reactive TCRs—unlike pathogen-reactive TCRs, which were more often classified as nonHvG—were disproportionately enriched in post-Tx BAL and TBBx samples compared to peripheral blood

during early rejection. This finding supports the potential for using HvG TCRs in combination with pathogen-reactive TCRs as diagnostic markers to distinguish early rejection from infection-driven inflammation. Such differentiation is frequently missed by histology-based diagnostics, often resulting in inappropriate immunosuppression and life-threatening complications.

Rejection and infection are often interrelated in transplantation. Overimmunosuppression to control rejection increases susceptibility to infection, but the relationship is bidirectional. The concept of 'heterologous immunity'—in which virus-specific T cells can cross-react with alloantigens to enhance alloimmunity—has been documented [45, 46]. Barrier organ transplants, particularly the lungs and intestines, are especially vulnerable due to their extensive and often hidden surface areas, making them prone to infection-related rejection [2, 47]. Beyond barrier organs, studies in rodent skin transplantation [48, 49] and human kidney transplantation [50] have shown that immune responses to commensal organisms and CMV, respectively, can promote graft rejection. These findings underscore the need for effective and balanced control of both infection and rejection to improve clinical outcomes across a wide range of solid organ transplants. The current criteria for diagnosing ACR in lung transplant recipients were originally developed in the 1990s, with the most recent update in 2007 [8, 51]. Given the rapid advancements in next-generation sequencing and the rise of multiomic technologies, the field is primed for the development of more precise, mechanism-driven diagnostic tools. To this end, we have established innovative, multidisciplinary platforms to elucidate the mechanisms of rejection and infection, paving the way for future refinement of diagnostic strategies.

Our study has several limitations. First, the small cohort of LuTx patients precluded meaningful multivariate analyses. Early sample collection was impacted by the COVID-19 pandemic, and

as a result, early post-Tx blood samples were not obtained from Pts 1 and 4. In addition, the limited availability of microbial-reactive TCRs in reference databases restricted our ability to map a broader repertoire within our dataset. Nonetheless, our findings establish proof-of-concept that this platform is informative for studying human transplantation immunology. To address the limitations of current microbial-reactive TCR annotation, computational approaches such as TCR similarity algorithms (e.g., GLIPH2) could be leveraged to expand identification, as we previously described [22]. However, functional assays remain the gold standard for confirming pathogen reactivity, which was beyond the scope of this study. The observed association between HvG TCRs and rejection was identified in only a subset of patients, which may be partially explained by the presence of subclinical or histologically undetectable rejection [52]. Importantly, even undiagnosed rejection may contribute to pulmonary function decline. Our findings indicate that lung-infiltrating HvG T cells may adversely affect pulmonary function regardless of clinically overt rejection. While clinical data were not always available or temporally aligned with TCR sequencing, our results suggest that incorporating early pulmonary function tests could enhance the interpretation of TCR-seq data and potentially predict the development of CLAD and mortality (e.g., Pts 4 and 13, Fig. 5D, Table S1). Validation of these findings in an expanded cohort will be necessary to confirm their generalizability and clinical utility. Both our current LuTx data (Fig. 5C: Pt9; Fig. S8B: Pt8) and our previous intestinal transplantation studies [21] found that pre-Tx MLR-defined HvG clones show diminished correlation with late-stage (POD>150) rejection episodes. A promising approach to enhance late rejection monitoring would involve additionally performing MLRs using post-Tx PBMCs or BAL-derived lymphocytes to enable detection of putative *de novo* HvG clones that develop post-Tx, similar to our intestinal transplantation findings [21]. However, such investigation extends beyond the current study scope.

Our data provides immunogenomic insights into the dynamic interplay between T cell alloreactivity and microbial reactivity in LuTx, advancing our understanding of rejection mechanisms and informing the refinement of diagnostic frameworks. By dissecting bidirectional alloresponses and tissue-residency dynamics, this study opens new avenues for future research focused on the development of precision therapies that selectively modulate alloimmune responses while preserving antimicrobial immunity—addressing a critical unmet need in improving LuTx outcomes.

Methods

Human subject recruitment and clinical protocols

The study was approved by the Columbia University Institutional Review Board (IRB #AAAS6206 & AAAR2681). All subjects or legal guardians provided their written, informed consent and assent when appropriate. Our cohort enrolled thirteen patients: six single-lung transplant recipients (Pts1, 2, 3, 7, 11, 12), six double-lung transplant recipients (Pts4, 5, 6, 8, 10, 13), and one double-lung-and-liver transplant recipient (Pt9). Because Pt2 and Pt5 passed away less than six months post-Tx and there were limited pre-Tx and post-Tx specimens collected from these patients, they were excluded from cohort analysis. All lung allografts were procured from donors after brain death without the use of Normothermic Regional Perfusion.

In the post-Tx period, rejection was graded following the International Society for Heart & Lung Transplantation (ISHLT) guidelines, with attention to acute rejection and airway inflammation [8]. Acute rejection was graded from none, minimal, mild, moderate, to severe, while small airways inflammation was graded as none, low grade, high grade, or ungradable. ACR is diagnosed by the presence of perivascular and interstitial mononuclear infiltrates in lung tissue (TBBx: transbronchial biopsies) and is graded by the severity of inflammation both in the vascular compartment (A0 to A4) and airway (B0 to B2R). Surveillance bronchoscopy with transbronchial biopsy was performed by physicians at 4–6 weeks, and then 3-, 6-, 9-, and 12-months post-Tx. Subsequent and/or additional bronchoscopies were performed as clinically needed. Blood samples were collected once weekly for the first 12 weeks, and subsequently at least once per month if available. Spirometry and chest radiographs were performed once a week for the first 12 weeks and subsequently at least once a month.

Initial immunosuppression for all LuTx patients consisted of induction therapy with basiliximab administered on post-operative day (POD) 0 and POD4 (each dose: 20 mg IV infused over 30 minutes), as well as methylprednisolone (1000 mg IV on POD0). Pre-operatively, tacrolimus was administered (2 mg PO x 1 for patient weight ≥ 50 kg, 1 mg PO x 1 for patient weight < 50 kg), and mycophenolate mofetil was administered (1000 mg PO x 1). LuTx patients followed a post-Tx maintenance regimen that included a calcineurin inhibitor (tacrolimus), antiproliferative agents (mycophenolate mofetil), and corticosteroids (methylprednisolone and prednisone). Tacrolimus was continued post-operatively and administered every 12 hours, adjusted to aim for a target trough level of 12–15 ng/mL during the first year post-Tx, and 10–15 ng/mL during subsequent years post-Tx. Methylprednisolone was also continued, with one 125 mg dose every 8 hours for 24 hours on POD1, followed by 0.5 mg/kg IV daily that was gradually tapered to 10 mg daily by POD90, and then ideally further tapered to 5–10 mg daily after 1–2 years post-Tx. Methylprednisolone was changed to oral prednisone (1:1) if the patient could tolerate oral medication. Mycophenolate mofetil was continued at 1000 mg PO/IV every 12 hours. In instances of allograft rejection, immunosuppression was tailored and administered based on the severity of rejection.

Bronchoalveolar lavage (BAL) cell isolations

BAL cells were isolated from surveillance bronchoscopy specimens or pre-Tx donor or recipient BAL samples when available. Specimens were centrifuged at 515g for 5 minutes at 4°C, the supernatant was then passed through a 40 μm filter. The filtrate was frozen at -80°C in a maximum of five 1mL aliquots, and the cell pellet was resuspended in 2mL of ACK lysis buffer, incubated for 3 minutes at room temperature, then centrifuged at 515g for 5 minutes at 4°C. The supernatant was discarded, and the cell pellet was resuspended in PBS, where it then passed

through another 40 μm filter, and then cell counting (focused on lymphocyte-looking cells) was performed on the filtrate using a hemocytometer under the microscope (BH2, Olympus). In rare cases, bronchoalveolar washing (BW) fluid was collected and the cell isolation was similar as to processing BAL cells except the supernatant was not collected after the initial spin and filtering process.

PBMC isolations

PBMCs were isolated from patient whole blood samples or pre-Tx donors or recipient whole blood samples when available. To isolate PBMCs, density gradient centrifugation was utilized. First, patient blood specimen was diluted in PBS at a 1:4 to 1:10 volume ratio. Histopaque was then added to fresh conical tubes, and the diluted blood was carefully layered on top of the Histopaque, keeping a clear separation between both layers. The volume ratio of Histopaque to dilute blood in each tube followed a ratio of 1:2. The tubes were then centrifuged at 400g for 30 minutes at 22°C, with acceleration set to 3 and brakes set to 0. The buffy coat was then carefully isolated, washed with PBS, treated with ACK lysis buffer, reconstituted with PBS, and then cell counting was performed using a hemocytometer under the microscope.

Lymphocyte isolation from pre-Tx donor and recipient lung-associated lymph nodes (LLNs)

The surgeon removed LLNs from the explanted lung(s), and lymphocytes were isolated from pre-Tx donor or recipient samples when available. Using forceps and scissors, samples were cut into small pieces (about 5 mm^2) and incubated for 1 hour at 37°C in culture medium (RPMI 1640, 1 mg/mL Collagenase D, and 100 IU/mL penicillin-streptomycin). After incubation, the

samples were filtered through a 100μm filter and resuspended in MLR medium (AIM-V media mixed with 5% AB heat-inactivated human serum, 0.01M Hepes, and 50 μm 2-mercaptoethanol) then centrifuged for 5 minutes at 515g. If the cell pellet appeared to contain red blood cells, it resuspended in 5 mL of ACK lysis buffer & incubated for 5 minutes on ice, then brought to 50 mL with 1x RPMI, then centrifuged again. The cell pellet was then resuspended in MLR media, passed through a 40 μm filter, and counted using a hemocytometer under the microscope (BH2, Olympus).

Lymphocyte isolation from pre-Tx lung explant tissues

Cells were isolated from patient pre-Tx lung explant tissues when available. Using forceps and scissors, lung tissues were cut into 4–10 mm^3 pieces and then treated for 1.5 hours at 37°C in sterile-filtered isolate buffer (RPMI 1640, 1 mg/mL Collagenase D, 100 IU/mL penicillin-streptomycin, 10 μg/mL DNAse, and 1 μg/mL Amphotericin B). Residual tissue pieces were further broken down using the gentleMACS Dissociator, and the supernatant was filtered. The filtrate was centrifuged at 450g for 10 minutes at 21°C and the cell pellet was resuspended in MLR medium (AIM-V media mixed with 5% AB heat-inactivated human serum, 0.01M Hepes, and 50 μm 2-mercaptoethanol). This resuspension was then mixed with an 88% isotonic Percoll solution (9:1:1.36 ratio of stock Percoll, 10X PBS, and 1X HBSS without Ca^{2+} respectively) at a 1:1 volume ratio. Lung tissue cells were then isolated from this mixture via density gradient centrifugation for 20 minutes at 800g for 20 minutes, with the brakes set to 0. The supernatant was aspirated, and the remaining cell pellet was treated with ACK lysis buffer before being washed, filtered, and counted using a hemocytometer under the microscope (BH2, Olympus).

Human leukocyte antigen (HLA) allotype-specific staining and cellular staining by flow cytometry

Based on the clinically available HLA typing for each LuTx donor and recipient (Table S2), various monoclonal HLA class I allotype-specific antibodies were selected and then assessed for their ability to discriminate between donor and pre-Tx recipient cells as we published previously [26]. During this quality control process, each HLA allotype-specific antibody was used in conjunction with pan-HLA-ABC antibody, and those that adequately discriminated between donor and pre-Tx recipient PBMCs were included when tailoring lineage-specific antibody panels for each LuTx patient (Table S2). Cellular staining was performed on up to 0.5M PBMCs or BAL cells from the patient sample and compared to healthy control PBMCs isolated from the blood product provided by the New York Blood Bank. Staining was performed in accordance with previous published protocol [26]. Briefly, 1mL of FACS buffer was added to each sample and then centrifuged at 465 g for 5 minutes at 4°C. The supernatant was poured off, then 2.5 µL of Fc block followed by 5 µL of each antibody in the patient's lineage-specific panel was added to each tube as the primary staining. Multiple flow cytometry antibodies were used in this process (Table S3). Following a 30-minute incubation at 4°C, the sample was centrifuged again after 1mL of FACS buffer was added, then the supernatant was poured off and cells were resuspended at $10x10^6$ cells/mL of FACS buffer before 5 µL of the secondary antibody was added and incubated at 4°C for 30 minutes. The samples were then centrifuged with 1 mL of FACS buffer, the supernatant was later poured off, and cells were resuspended in FACS buffer before the final step where 2.5 µL of DAPI (2ug/ml stock) was added. Cells were kept at 4°C (for a maximum of 12 hours) before acquisition on either the BD LSR II flow cytometer or the Cytek Aurora flow cytometer. Data analysis was performed using FlowJo software (V10.10.0, BD Biosciences).

Carboxyfluorescein succinimidyl ester (CFSE)-mixed lymphocyte reactions (MLRs) and cell sorting

LuTx MLR assays were performed as described previously [18, 53]. GvH and HvG MLRs were set up with thawed pre-Tx donor and pre-Tx recipient LLN cells. In each MLR, 200,000 CFSE-labeled responders and 200,000 violet-dye-labeled irradiated (35 Gy, X-RAD320) stimulators in MLR medium (AIM-V media mixed with 5% AB heat-inactivated human serum, 0.01M Hepes, and 50 μm 2-mercaptoethanol) were plated together in wells of a round-bottom 96-well plate. After incubation at 37°C for six days, the cultures were harvested, and the cells were stained with an antibody panel including DAPI, CD45 V500, CD3 PerCP-Cy5.5, γδTCR PE-Cy7, CD4 redfluor 710 and CD8 APC-Cy7. Then, the cells underwent FACS sorting on a BD Influx cell sorter to isolate four violet-dye-negative, DAPI negative, CD45 positive cell populations: $CD3^{+}\gamma\delta TCR^{-}CD4^{+}CFSE^{low}$ and $CD3^{+}\gamma\delta TCR^{-}CD8^{+}CFSE^{low}$, which represent the proliferated $CD4^{+}$ and $CD8^{+}$ T cells, and $CD3^{+}\gamma\delta TCR^{+}CFSE^{low}$, and $CD3^{+}\gamma\delta TCR^{+}CFSE^{high}$, which represent the proliferated and non-proliferated γδTCR T cells for other projects.

DNA extraction and TCRβ CDR3 DNA sequencing

Genomic DNA was isolated from different tissue types from LuTx patients and their donors using the QIAGEN DNeasy Blood and Tissue Kit. FFPE tissue curls of post-Tx lung bronchoscopy specimens were requested from the Pathology Core at the Columbia University Irving Medical Center in order to extract genomic DNA, and the QIAGEN DNA FFPE Tissue Kit was used to isolate the DNA. Purity and yield of all DNA samples were assessed on the Nanodrop (Thermo Fisher Scientific). The DNA was frozen at -20°C and shipped on dry ice to Adaptive Biotechnologies for high-throughput TCRβ sequencing. Samples for TCRβ sequencing were summarized in Fig. S2.

TCRβ CDR3 data processing and analysis

TCR sequencing data was retrieved from Adaptive Biotechnology's ImmunoSEQ Annalyzer. Data analysis followed our previously published method [19, 21, 23]. Briefly, CD8 versus CD4 sorting error was corrected by removing sequences detected in both populations at high to low frequency ratio less than 5:1. Donor- and recipient-shared CDR3s at the nucleotide level were removed due to not being clearly assigned to either origin. Separate CD4 and CD8 tables containing clonal frequencies in pre-Tx unstimulated samples, $CFSE^{low}$ stimulated cells, and post-Tx samples were compiled and renormalized. Alloreactive clones were defined by 2-fold or greater expansion in stimulated compared with unstimulated pre-Tx cells by minimum frequency of 0.002% in $CFSE^{low}$ populations when using template counts, which serves to ensure 85% repeatability, as determined by power analysis. Mappable clones refer to clones that were detectable in sequenced pre-Tx lung, lymph node, and/or MLR $CFSE^{low}$ populations from the donor or recipients. Cumulative frequency was calculated as a percentage of all sequences weighted by copy numbers in designated populations (Table S4). The unique clone numbers of mappable clones, mappable alloreactive clones, and the cumulative frequency of alloreactive clone of post-Tx samples were summarized in Table S5. The number of pathogen-reactive TCRs collected from public available database were listed in Table S6 [27-32].

Software and Statistical Analysis

R (R-4.4.3) and RStudio (2024.12.1) were used to analyze TCR-seq data and generate circle plots. GraphPad Prism (v 10.4.2, GraphPad Software) was used to produce figures. A Shapiro–Wilk test was performed to determine normality of data distributions. For the two unpaired data sets that meet the assumption of a normal distribution, a parametric unpaired t test was

performed. For the two paired data sets that meet the assumption of a normal distribution, a parametric paired t test was performed. For the two paired data sets that didn't meet the assumption of a normal distribution, a non-parametric Wilcoxon test was performed to compare the median ranks. A non-parametric Kruskal–Wallis test followed by Dunn's multiple comparisons test was performed for comparisons among three or more unpaired independent groups that didn't meet the assumption of a normal distribution, to compare the median ranks. For three or more independent groups with paired data that didn't follow the assumption of a normal distribution, a non-parametric Friedman test followed by Dunn's multiple comparisons test was performed.

Data and materials availability

Raw TCRβ-seq data are available at https://clients.adaptivebiotech.com and a review account will be available for peer review. The R code used to analyze TCRβ-seq data is available in the GitHub repository at https://github.com/drjiaowy/LuTx_manuscript.git.

Acknowledgements

We thank the Flow Cytometry Core and Human Studies Core at Columbia Center for Translational Immunology (CCTI) for their excellent services. We gratefully acknowledge the generosity of the donor families, our LuTx patients and their families for making this study possible.

Funding

The study is supported by the Thomas Kully Immunology Fund and the Nelson Family Transplant Innovation Award Program at the Columbia University Irving Medical Center (to J.F.). W.J. was supported by the Nelson Family Transplant Fellowship and Innovation Award at Columbia University Irving Medical Center. Research reported here was performed in the CCTI Flow Cytometry Core, supported in part by the Office of the Director, National Institutes of Health (NIH) awards S10OD030282 and S10OD020056.

Author contributions

J.F. designed the study. W.J., K.D.L., T.Y., J.H.W. and J.F. performed the experiments. C.B.M., A.P.R., M.K., V.M., K.R., A.V., J.C., L.B., J.S., P.L., F.D., S.A. and J.F. coordinated the clinical sample and data collection. J.S., P.L. and F.D. performed the lung transplantation. L.B. and S.A. performed the routine patient care. W.J., K.D.L., T.Y., J.H.W. and J.F. performed data analysis. W.J. and J.F. wrote the codes to identify and track alloreactive and microbial reactive TCR clones. W.J. and J.F. wrote the final report. All authors contributed to the editing of the final report. All authors agree to all the content of the submitted manuscript.

Declaration of interests

J.F. served as a Scientific Consultant for Adaptive Biotechnologies from June 2022 to May 2023.

Privacy Statement

Identification numbers for patients and deceased organ donors are not known to anyone outside the research group.

Reference

1. Hartert, M., et al., *Lung transplantation: a treatment option in end-stage lung disease.* Deutsches Arzteblatt international, 2014. **111**(7): p. 107-116.
2. Valapour, M., et al., *OPTN/SRTR 2023 Annual Data Report: Lung.* Am J Transplant, 2025. **25**(2s1): p. S422-s489.
3. DeFreitas, M.R., et al., *Complications of Lung Transplantation: Update on Imaging Manifestations and Management.* Radiology. Cardiothoracic imaging, 2021. **3**(4): p. e190252-e190252.
4. Van Herck, A., et al., *Prevention of chronic rejection after lung transplantation.* J Thorac Dis, 2017. **9**(12): p. 5472-5488.
5. Mrad, A. and R.K. Chakraborty, *Lung Transplant Rejection*, in *StatPearls*. 2021, StatPearls Publishing LLC.: Treasure Island (FL).
6. Burton, C.M., et al., *Minimal acute cellular rejection remains prevalent up to 2 years after lung transplantation: a retrospective analysis of 2697 transbronchial biopsies.* Transplantation, 2008. **85**(4): p. 547-53.
7. Thabut, G. and H. Mal, *Outcomes after lung transplantation.* J Thorac Dis, 2017. **9**(8): p. 2684-2691.
8. Stewart, S., et al., *Revision of the 1996 working formulation for the standardization of nomenclature in the diagnosis of lung rejection.* J Heart Lung Transplant, 2007. **26**(12): p. 1229-42.
9. Arcasoy, S.M., et al., *Pathologic interpretation of transbronchial biopsy for acute rejection of lung allograft is highly variable.* Am J Transplant, 2011. **11**(2): p. 320-8.
10. Bhorade, S.M., et al., *Interobserver variability in grading transbronchial lung biopsy specimens after lung transplantation.* Chest, 2013. **143**(6): p. 1717-1724.
11. Bergantini, L., et al., *Regulatory and Effector Cell Disequilibrium in Patients with Acute Cellular Rejection and Chronic Lung Allograft Dysfunction after Lung Transplantation: Comparison of Peripheral and Alveolar Distribution.* Cells, 2021. **10**(4): p. 780.
12. Slebos, D.-J., et al., *Bronchoalveolar lavage fluid characteristics in acute and chronic lung transplant rejection.* The Journal of Heart and Lung Transplantation, 2004. **23**(5): p. 532-540.
13. Shino, M.Y., et al., *The Prognostic Importance of Bronchoalveolar Lavage Fluid CXCL9 During Minimal Acute Rejection on the Risk of Chronic Lung Allograft Dysfunction.* American Journal of Transplantation, 2018. **18**(1): p. 136-144.
14. Keller, M. and S. Agbor-Enoh, *Cell-free DNA in lung transplantation: research tool or clinical workhorse?* Curr Opin Organ Transplant, 2022. **27**(3): p. 177-183.
15. Zuber, J., et al., *Bidirectional intragraft alloreactivity drives the repopulation of human intestinal allografts and correlates with clinical outcome.* Science Immunology, 2016. **1**(4): p. eaah3732.
16. Savage, T.M., et al., *Early expansion of donor-specific Tregs in tolerant kidney transplant recipients.* JCI Insight, 2018. **3**(22).
17. Fu, J., et al., *Human Intestinal Allografts Contain Functional Hematopoietic Stem and Progenitor Cells that Are Maintained by a Circulating Pool.* Cell Stem Cell, 2019. **24**(2): p. 227-239.
18. Fu, J., et al., *Lymphohematopoietic graft-versus-host responses promote mixed chimerism in patients receiving intestinal transplantation.* J Clin Invest, 2021. **131**(8).
19. Obradovic, A., et al., *Integrated analysis toolset for defining and tracking alloreactive T-cell clones after human solid organ and hematopoietic stem cell transplantation.* Software Impacts, 2021. **10**: p. 100142.
20. Fu, J., M. Khosravi-Maharlooei, and M. Sykes, *High Throughput Human T Cell Receptor Sequencing: A New Window Into Repertoire Establishment and Alloreactivity.* Frontiers in Immunology, 2021. **12**(4677).
21. Fu, J., et al., *Plasticity of intragraft alloreactive T cell clones in human gut correlates with transplant outcomes.* J Exp Med, 2024. **221**(1).
22. Fu, J., et al., *T cell repertoire profiling in allografts and native tissues in recipients with COVID-19 after solid organ transplantation: Insight into T cell-mediated allograft protection from viral infection.* Front Immunol, 2022. **13**: p. 1056703.
23. Jiao, W., et al., *Dynamic establishment of recipient resident memory T cell repertoire after human intestinal transplantation.* EBioMedicine, 2024. **101**: p. 105028.
24. Snyder, M.E., et al., *Generation and persistence of human tissue-resident memory T cells in lung transplantation.* Sci Immunol, 2019. **4**(33).

25. Snyder, M.E., et al., *Modulation of tissue resident memory T cells by glucocorticoids after acute cellular rejection in lung transplantation.* Journal of Experimental Medicine, 2022. **219**(4).
26. Long, K.D. and J. Fu, *Chimerism and phenotypic analysis of intraepithelial and lamina propria T cells isolated from human ileal biopsies after intestinal transplantation.* STAR Protoc, 2023. **4**(2): p. 102192.
27. Napolitani, G., et al., *Clonal analysis of Salmonella-specific effector T cells reveals serovar-specific and cross-reactive T cell responses.* Nat Immunol, 2018. **19**(7): p. 742-754.
28. Cassotta, A., et al., *Broadly reactive human CD4(+) T cells against Enterobacteriaceae are found in the naïve repertoire and are clonally expanded in the memory repertoire.* Eur J Immunol, 2021. **51**(3): p. 648-661.
29. Chen, S.Y., et al., *TCRdb: a comprehensive database for T-cell receptor sequences with powerful search function.* Nucleic Acids Res, 2021. **49**(D1): p. D468-d474.
30. Shugay, M., et al., *VDJdb: a curated database of T-cell receptor sequences with known antigen specificity.* Nucleic Acids Res, 2018. **46**(D1): p. D419-d427.
31. Zhang, W., et al., *PIRD: Pan immune repertoire database.* 2019.
32. Rambo-Martin, B., K. Lacek, and R. Chau, *MIRA: An Interactive Dashboard for Influenza Genome and SARS-CoV-2 Spike-Gene Assembly and Curation.* 2023.
33. Fu, J. and M. Sykes, *Emerging Concepts of Tissue-resident Memory T Cells in Transplantation.* Transplantation, 2021.
34. Beura, L.K., et al., *T Cells in Nonlymphoid Tissues Give Rise to Lymph-Node-Resident Memory T Cells.* Immunity, 2018. **48**(2): p. 327-338.e5.
35. Behr, F.M., et al., *Tissue-resident memory CD8(+) T cells shape local and systemic secondary T cell responses.* Nat Immunol, 2020. **21**(9): p. 1070-1081.
36. Strobl, J., et al., *Human resident memory T cells exit the skin and mediate systemic Th2-driven inflammation.* J Exp Med, 2021. **218**(11).
37. Künzli, M. and C.G. King, *Resident Memory T Cells Escape 'Home Quarantine'.* Trends Immunol, 2020. **41**(6): p. 454-456.
38. Fonseca, R., et al., *Developmental plasticity allows outside-in immune responses by resident memory T cells.* Nat Immunol, 2020. **21**(4): p. 412-421.
39. Gebhardt, T., et al., *Different patterns of peripheral migration by memory CD4+ and CD8+ T cells.* Nature, 2011. **477**(7363): p. 216-219.
40. Collins, N., et al., *Skin CD4+ memory T cells exhibit combined cluster-mediated retention and equilibration with the circulation.* Nature Communications, 2016. **7**(1): p. 11514.
41. Klicznik, M.M., et al., *Human CD4⁺CD103⁺ cutaneous resident memory T cells are found in the circulation of healthy individuals.* Science Immunology, 2019. **4**(37): p. eaav8995.
42. Sgambelluri, F., et al., *A role for CCR5(+)CD4 T cells in cutaneous psoriasis and for CD103(+) CCR4(+) CD8 Teff cells in the associated systemic inflammation.* J Autoimmun, 2016. **70**: p. 80-90.
43. Han, A., et al., *Dietary gluten triggers concomitant activation of CD4+ and CD8+ αβ T cells and γδ T cells in celiac disease.* Proc Natl Acad Sci U S A, 2013. **110**(32): p. 13073-8.
44. DeWolf, S., et al., *Quantifying size and diversity of the human T cell alloresponse.* JCI Insight, 2018. **3**(15).
45. Amir, A.L., et al., *Allo-HLA reactivity of virus-specific memory T cells is common.* Blood, 2010. **115**(15): p. 3146-57.
46. Karahan, G.E., F.H.J. Claas, and S. Heidt, *Heterologous Immunity of Virus-Specific T Cells Leading to Alloreactivity: Possible Implications for Solid Organ Transplantation.* Viruses, 2021. **13**(12): p. 2359.
47. Horslen, S.P., et al., *OPTN/SRTR 2023 Annual Data Report: Intestine.* Am J Transplant, 2025. **25**(2s1): p. S288-s328.
48. Pirozzolo, I., et al., *Host-versus-commensal immune responses participate in the rejection of colonized solid organ transplants.* J Clin Invest, 2022. **132**(17).
49. Lei, Y.M., et al., *Skin-restricted commensal colonization accelerates skin graft rejection.* JCI Insight, 2019. **5**(15).
50. Stranavova, L., et al., *Heterologous Cytomegalovirus and Allo-Reactivity by Shared T Cell Receptor Repertoire in Kidney Transplantation.* Front Immunol, 2019. **10**: p. 2549.
51. Yousem, S.A., et al., *Revision of the 1990 working formulation for the classification of pulmonary allograft rejection: Lung Rejection Study Group.* J Heart Lung Transplant, 1996. **15**(1 Pt 1): p. 1-15.
52. Rush, D., *Subclinical Rejection: a Universally Held Concept?* Current Transplantation Reports, 2020. **7**.

53. Fu, J. and M. Sykes, *CFSE-MLR and cell sorting protocol to define alloreactive T cell repertoires by high throughput TCR sequencing.* Bio-protocol Preprint, 2023.

Fig. 1 Dynamic establishment of recipient TCR repertoires in BAL and PBMCs. (A) Percentages of donor and recipient CD8+ T cells with TRM phenotypes (CD69+ CD103+) among all the patients (n=11) who underwent post-Tx BAL sample analysis by flow cytometry. (B) Comparison of donor and recipient CD8+ T cell percentages with TRM phenotypes. Samples were stratified into three groups based on postoperative day (POD). (C) Jensen-Shannon Divergence (JSD) values between adjacent sampling time points in BAL and PBMC from patients' (n=8). (D) Pre-Tx-detected recipient TCRs and post-Tx newly detected TCRs contributed to the TCR repertoires of BAL and PBMCs in Pt8. All the per-Tx samples (listed in Fig. S2), including BAL, lung, PBMC, lung-associated lymph nodes (LLN), and spleen, were used to define the pre-Tx-detected TCRs. In panel D and Fig. S4, pre-Tx-detected donor TCRs (data not shown), pre-Tx-detected recipient TCRs, and post-Tx newly detected TCRs collectively account for 100% of each sample. (E) Recurrence proportions of TCR subsets (defined in D) by unique sequence count (unweighted) post-Tx. Each TCR subset (except those detected at the last sampling time) has a corresponding recurrence proportion group. (F) Comparison of recurrence between the earliest pre-Tx-detected recipient TCR subset and the earliest post-Tx newly detected TCR subset per patient. Recurrence values were normalized by the area under curve (AUC) divided by the time span (shown in E and Fig.S4C). Unpaired t test was performed for panel B. Wilcoxon test and Paired t test were performed for the upper and lower plots, respectively. Solid horizontal bars indicate means, and dotted horizontal bars indicate medians. **$p < 0.01$, ****$p < 0.0001$.

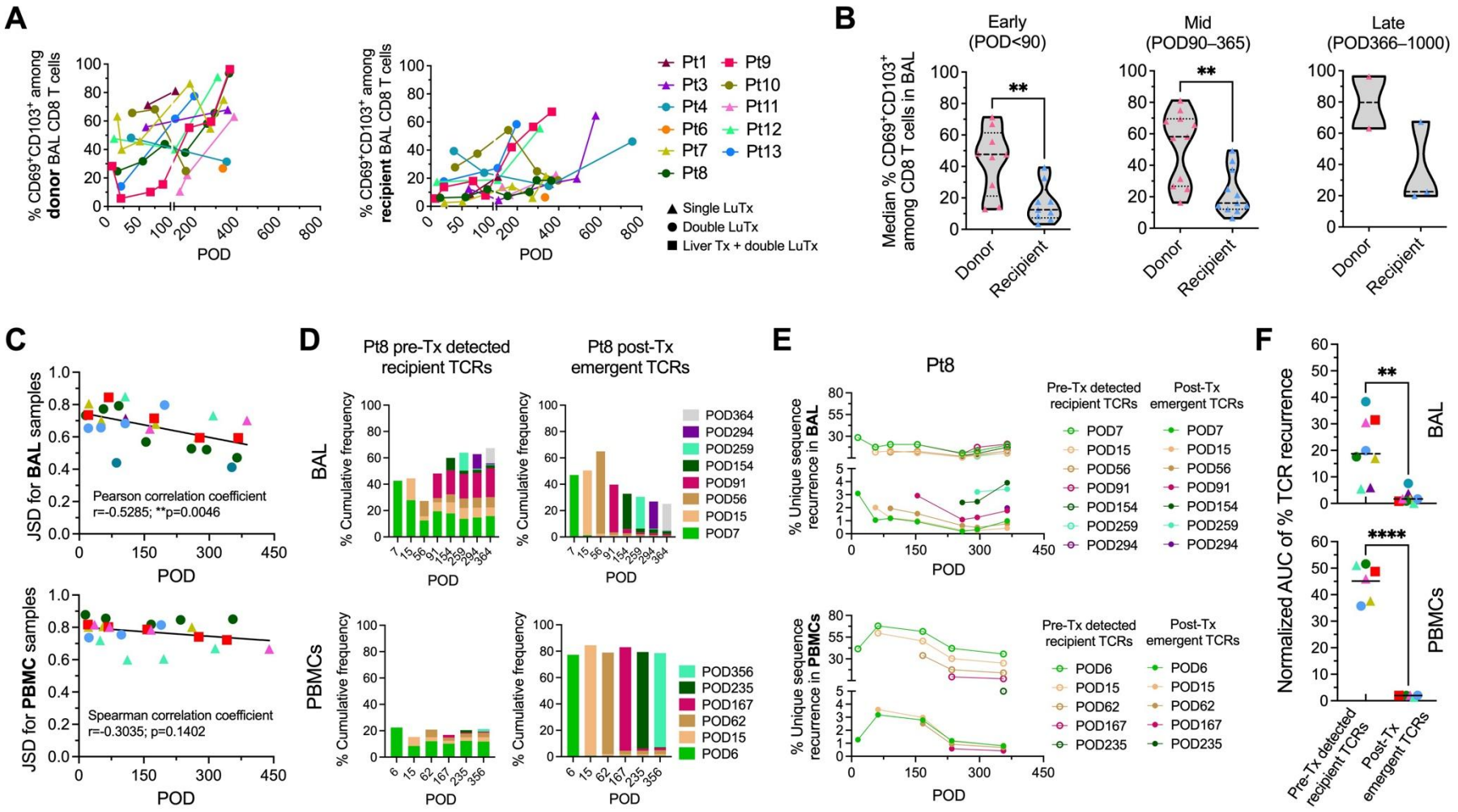
A
% CD69+CD103+ among donor BAL CD8 T cells
% CD69+CD103+ among recipient BAL CD8 T cells
POD
Pt1
Pt3
Pt4
Pt6
Pt7
Pt8
Pt9
Pt10
Pt11
Pt12
Pt13
Single LuTx
Double LuTx
Liver Tx + double LuTx
B
Early (POD<90)
Mid (POD90–365)
Late (POD366–1000)
Median % CD69+CD103+ among CD8 T cells in BAL
Donor
Recipient
C
JSD for BAL samples
Pearson correlation coefficient
r=-0.5285; **p=0.0046
JSD for PBMC samples
Spearman correlation coefficient
r=-0.3035; p=0.1402
D
Pt8 pre-Tx detected recipient TCRs
Pt8 post-Tx emergent TCRs
BAL
PBMCs
% Cumulative frequency
POD364
POD294
POD259
POD154
POD91
POD56
POD15
POD7
POD356
POD235
POD167
POD62
POD6
E
Pt8
% Unique sequence recurrence in BAL
% Unique sequence recurrence in PBMCs
Pre-Tx detected recipient TCRs
Post-Tx emergent TCRs
F
Normalized AUC of % TCR recurrence
BAL
PBMCs
Pre-Tx detected recipient TCRs
Post-Tx emergent TCRs

Fig. 2 Composition, relative detection rate, and persistence of T cell subsets by tissue origin. (A) Cumulative frequencies of recipient TCRs classified as “lymphoid-PBMC-lung shared” (1), “PBMC-lung shared” (2), “lymphoid-lung shared” (3), “lymphoid-PBMC shared” (4), “lung only” (5), “PBMC only” (6), and “lymphoid only” (7) in pre-Tx and post-Tx samples. R4U: recipient CD4 unstimulated; R8U: recipient CD8 unstimulated; R4L: recipient CD4 CFSE ^{low}; R8L: recipient CD8 CFSE^{low}. (B) Relative detection rates in post-Tx Pt8 BAL and Pt8 PBMC for sequences identified pre-Tx. The relative detection rate (odds ratio) compares the detection rate of two sequence subsets. A value > 1 indicates a higher detection of the first subset versus the second. (C) Time-normalized AUC of all relative detection rate values. (D) Representative circle plots of TCR subsets in Pt8 BAL and PBMC: “lymphoid only” (non-shared TCRs), “lymphoid-PBMC shared” (double shared TCRs), and “lymphoid-PBMC-lung shared”. Colored line lengths represent the % overlap (cumulative frequency, 0–100) between the sampling timepoint (line) and the reference timepoint (outside circle label) The latter serves as the denominator. (E) Median overlap % among TCR subsets, stratified by pre-Tx detection, across all patients’ post-Tx BAL and PBMC samples. The Friedman test followed by Dunn’s multiple comparisons test was performed for panels C and E. Solid horizontal bars indicate means and dotted horizontal bars indicate medians. *$p < 0.05$, **$p < 0.01$, ***$p < 0.001$, ****$p < 0.0001$.

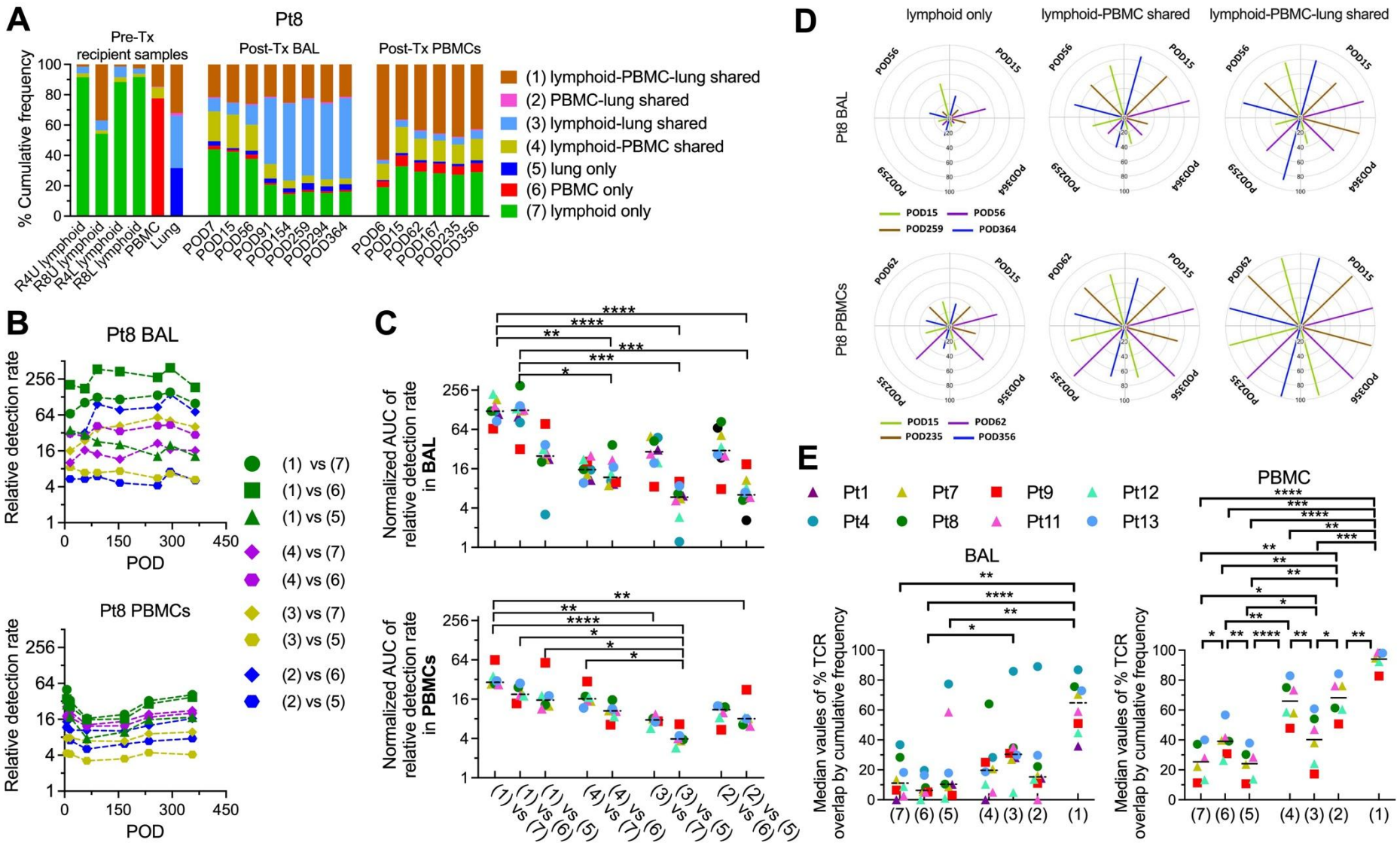
A
Pt8
Pre-Tx recipient samples
Post-Tx BAL
Post-Tx PBMCs
% Cumulative frequency
(1) lymphoid-PBMC-lung shared
(2) PBMC-lung shared
(3) lymphoid-lung shared
(4) lymphoid-PBMC shared
(5) lung only
(6) PBMC only
(7) lymphoid only
R4U lymphoid
R8U lymphoid
R4L lymphoid
R8L lymphoid
PBMC
Lung
POD7
POD15
POD56
POD91
POD154
POD259
POD294
POD364
POD6
POD15
POD62
POD167
POD235
POD356
B
Pt8 BAL
Relative detection rate
POD
Pt8 PBMCs
(1) vs (7)
(1) vs (6)
(1) vs (5)
(4) vs (7)
(4) vs (6)
(3) vs (7)
(3) vs (5)
(2) vs (6)
(2) vs (5)
C
Normalized AUC of relative detection rate in BAL
Normalized AUC of relative detection rate in PBMCs
D
lymphoid only
lymphoid-PBMC shared
lymphoid-PBMC-lung shared
Pt8 BAL
Pt8 PBMCs
POD15
POD56
POD259
POD364
POD62
POD235
POD356
E
Pt1
Pt7
Pt9
Pt12
Pt4
Pt8
Pt11
Pt13
BAL
PBMC
Median vaules of % TCR overlap by cumulative frequency

Fig. 3 Crosstalk between PBMC and BAL samples and the differences among TCR subsets. (A) Representative correlation plots of clone frequencies between paired BAL and PBMC samples from Pt8. (B) BAL and PBMC samples were grouped into 9 pairs based on sampling dates. The median cumulative frequency of shared sequences in BAL of each patient in each group were summarized and compared across early (group A, B, C), mid (group D, E, F) and late (G, H, I) periods of BAL sampling. (C) Comparison of PBMC-BAL overlapping percentages between pre-Tx-detected recipient TCRs and post-Tx newly detected TCRs when compiled all 9 pairs (defined in panel B). (D) Comparison of PBMC-BAL-overlapping percentages among pre-Tx detectable recipient TCR subsets by tissue origin (defined in Fig. 2) when compiled all 9 pairs (defined in panel B). (E) Comparison of PBMC-BAL overlapping percentages among CD4 and CD8 HvG and nonHvG TCRs when compiled all 9 pairs (defined in panel B). Kruskal-Wallis test followed by Dunn's multiple comparisons test was performed for panel B. Wilcoxon test was performed for panel C. Friedman test followed by Dunn's multiple comparisons test were performed for panels D and E. Dotted horizontal bars indicate medians. *$p < 0.05$, ***$p < 0.001$, ****$p < 0.0001$.

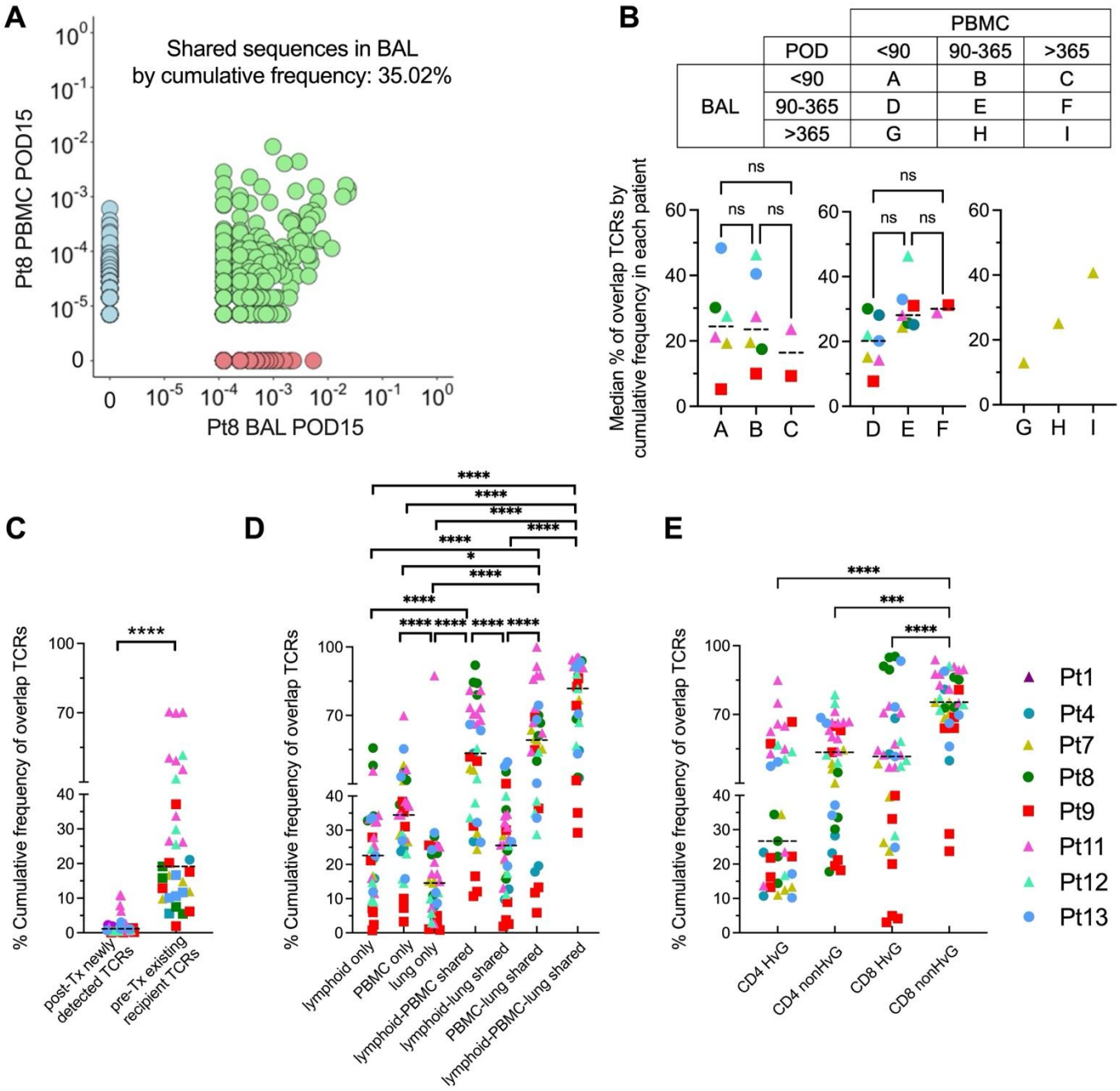
A
Shared sequences in BAL
by cumulative frequency: 35.02%
Pt8 PBMC POD15
Pt8 BAL POD15
B
PBMC
POD
<90
90-365
>365
BAL
<90
90-365
>365
A
B
C
D
E
F
G
H
I
Median % of overlap TCRs by cumulative frequency in each patient
ns
C
% Cumulative frequency of overlap TCRs
post-Tx newly detected TCRs
pre-Tx existing recipient TCRs
D
lymphoid only
PBMC only
lung only
lymphoid-PBMC shared
lymphoid-lung shared
PBMC-lung shared
lymphoid-PBMC-lung shared
E
CD4 HvG
CD4 nonHvG
CD8 HvG
CD8 nonHvG
Pt1
Pt4
Pt7
Pt8
Pt9
Pt11
Pt12
Pt13

Fig. 4 Pathogen-driven TCR proportions and reactivity among TCR subsets with different alloreactivities. (A) Cumulative frequency proportion of EBV-reactive TCRs in post-Tx TBBx, PBMC and BAL samples of Pt9 and Pt13. The proportion of pre-Tx defined CD8 nonHvG TCRs among EBV-reactive TCRs in designated samples were annotated in the plots. (B) Median cumulative frequency (%) of designated pathogen-reactive TCRs in local (lung/ BAL) versus circulating compartments from 4 applicable patients with or without specific infection (CMV/EBV). "With" infection" samples were collected within ± 30 days of clinical diagnosis. (C) Composition of pathogen-reactive TCRs in Pt13 at the unique sequence level subgrouped by alloreactive vs nonalloreactive identification in pre-Tx MLRs, including CD4 and CD8 GvH and nonGvH, HvG and nonHvG categories. Pie chart centers indicate total unique TCRs reactive to each pathogen in all samples sequenced from Pt13. (D) Cumulative frequency of pathogen-reactive TCRs in post-Tx samples (n=8 patients), stratified by alloreactive (CD4 HvG, CD8 HvG, CD4 GvH, CD8 GvH) vs nonalloractive (CD4 nonHvG, CD8 nonHvG, CD4 nonGvH, CD8 nonGvH) identification. Wilcoxon tests were performed for panels B and D. Dotted horizontal bars indicate medians. *$p < 0.05$, **$p < 0.01$, ***$p < 0.001$, ****$p < 0.0001$. EBV: Epstein-Barr virus; CMV: cytomegalovirus; MTB: mycobacterium tuberculosis; SA: staphylococcus aureus; KP: klebsiella pneumoniae; EC: Escherichia coli; Shi: shigella; EA: Enterobacter aerogenes; YFV: yellow fever virus; HIV: human immunodeficiency virus; HCV: hepatitis C virus.

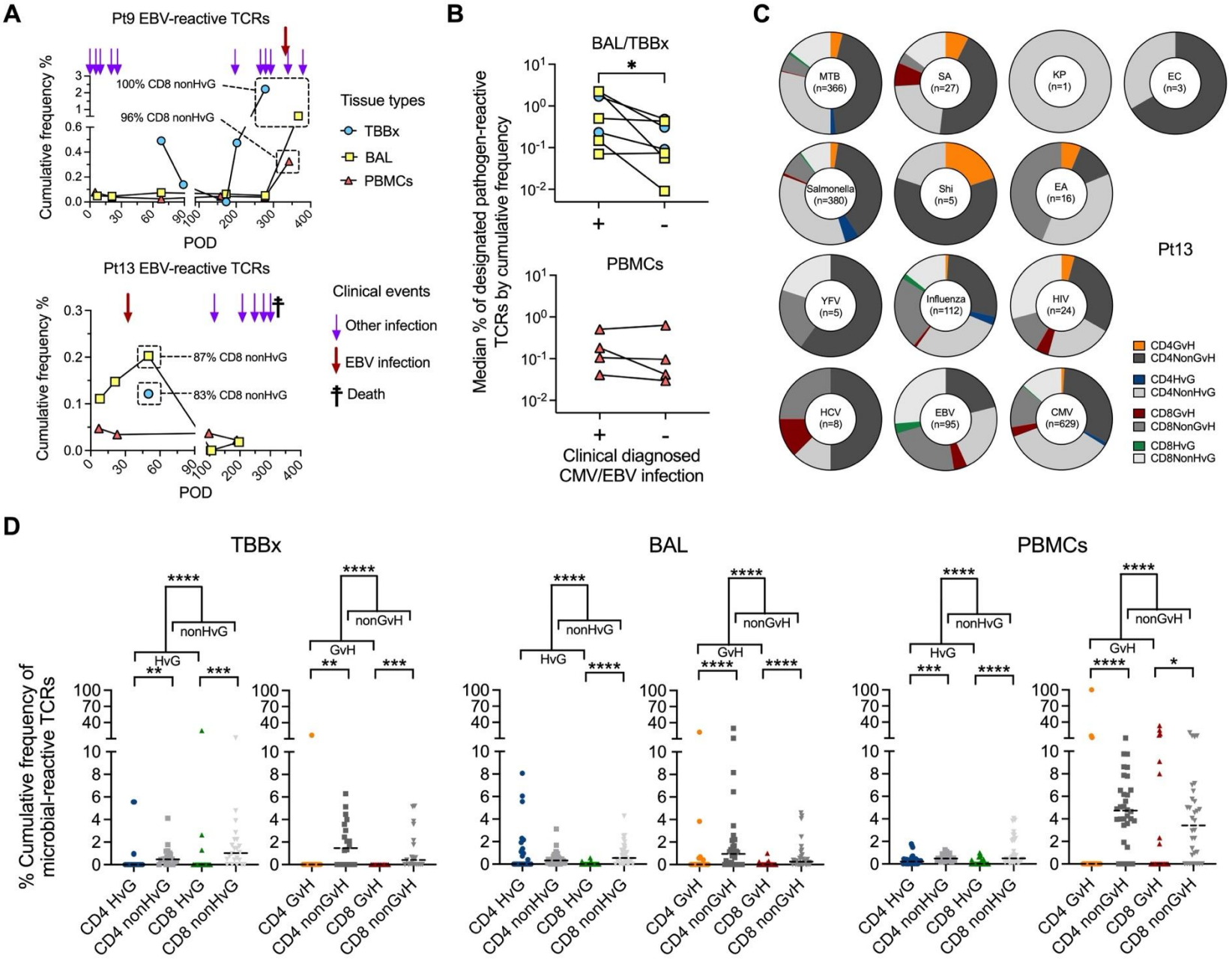
A
Pt9 EBV-reactive TCRs
Cumulative frequency %
100% CD8 nonHvG
96% CD8 nonHvG
POD
Tissue types
TBBx
BAL
PBMCs
Pt13 EBV-reactive TCRs
87% CD8 nonHvG
83% CD8 nonHvG
Clinical events
Other infection
EBV infection
Death
B
BAL/TBBx
PBMCs
Median % of designated pathogen-reactive TCRs by cumulative frequency
Clinical diagnosed CMV/EBV infection
C
MTB (n=366)
SA (n=27)
KP (n=1)
EC (n=3)
Salmonella (n=380)
Shi (n=5)
EA (n=16)
YFV (n=5)
Influenza (n=112)
HIV (n=24)
HCV (n=8)
EBV (n=95)
CMV (n=629)
Pt13
CD4GvH
CD4NonGvH
CD4HvG
CD4NonHvG
CD8GvH
CD8NonGvH
CD8HvG
CD8NonHvG
D
TBBx
BAL
PBMCs
% Cumulative frequency of microbial-reactive TCRs
HvG
nonHvG
GvH
nonGvH
CD4 HvG
CD4 nonHvG
CD8 HvG
CD8 nonHvG
CD4 GvH
CD4 nonGvH
CD8 GvH
CD8 nonGvH

Fig. 5 Relationship between TCR repertoire features and clinical outcomes. (A) Cumulative frequency of GvH and HvG clones in BAL specimens from representative patients. (B) Normalized area under the curve (AUC) analysis of GvH and HvG clones across all patients (Y-axis), with normalization by days of measurement (POD_{last} - POD_{first}). The X-axis shows similarly normalized AUC values for recipient T cell replacement (from Fig. S1C). (C) Percentage cumulative frequency of HvG-reactive sequences among recipient mappable repertoires in post-Tx PBMC, BAL and lung or liver allografts in representative patients. (D) According to the HvG in BAL over POD curves (Figs. 5C, S8B), three phases were defined as peak (circle), decline (reverse triangle) and baseline (square) (Fig. S8C) and the median of % cumulative frequency of HvG among recipient mappable repertoires in BAL was calculated for each patient (x axis). This is further associated with the pulmonary functions reflected by the median of % FEV1/baseline FEV1 values of each patient (y axis). FEV1: forced expiratory volume in one second. Pearson correlation analysis was performed for panel B (data follow normal distribution). Spearman correlation analysis was performed for panel D (data did not follow normal distribution). *$p < 0.05$, **$p < 0.01$.

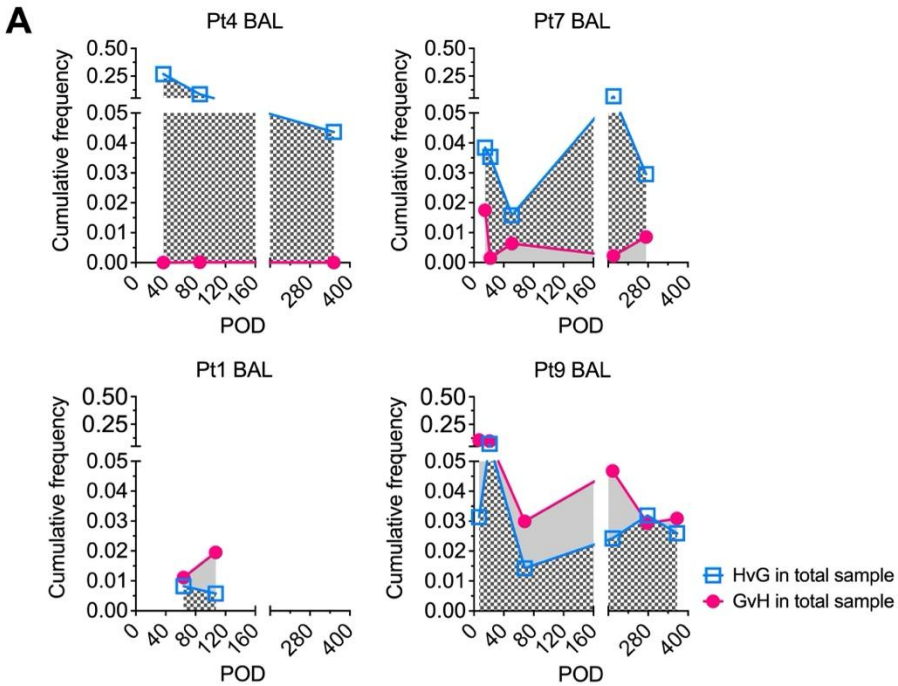
A
Pt4 BAL
Pt7 BAL
Pt1 BAL
Pt9 BAL
Cumulative frequency
POD
HvG in total sample
GvH in total sample

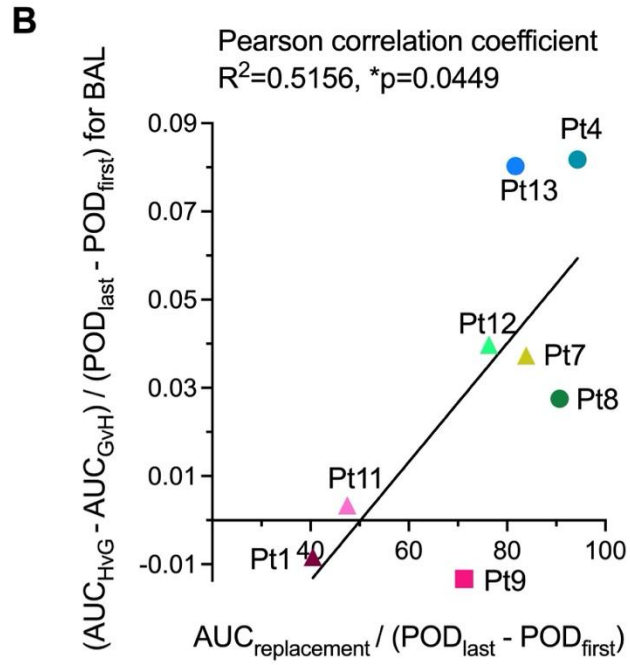
B
Pearson correlation coefficient
R2=0.5156, *p=0.0449
Pt4
Pt13
Pt12
Pt7
Pt8
Pt11
Pt1
Pt9
(AUCHvG - AUCGvH) / (PODlast - PODfirst) for BAL
AUCreplacement / (PODlast - PODfirst)

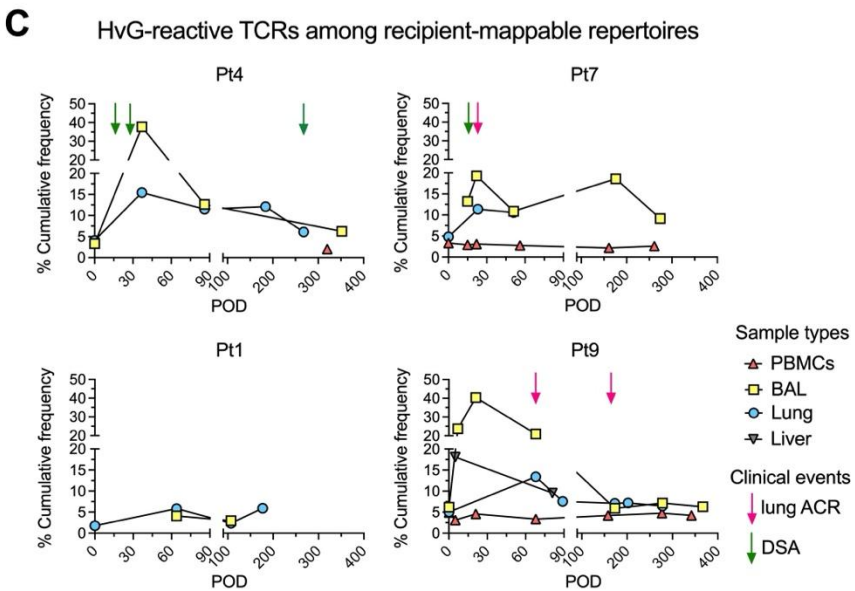
C
HvG-reactive TCRs among recipient-mappable repertoires
Pt4
Pt7
Pt1
Pt9
% Cumulative frequency
POD
Sample types
PBMCs
BAL
Lung
Liver
Clinical events
lung ACR
DSA

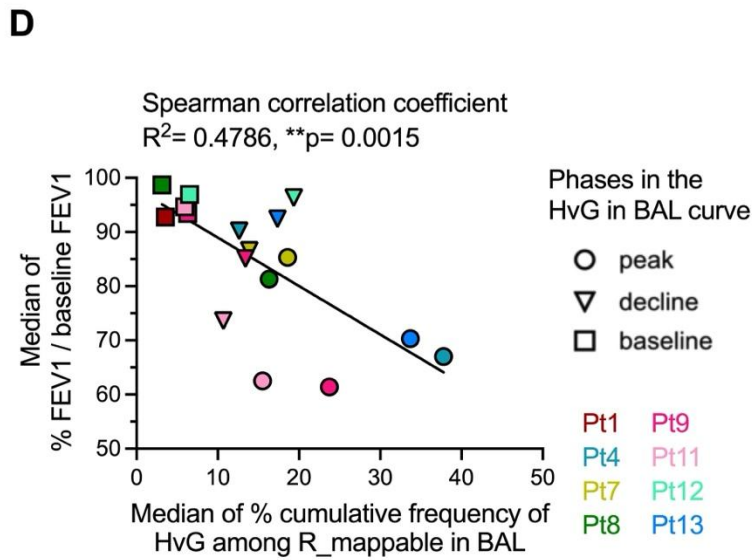
D
Spearman correlation coefficient
R2= 0.4786, **p= 0.0015
Median of % FEV1 / baseline FEV1
Median of % cumulative frequency of HvG among R_mappable in BAL
Phases in the HvG in BAL curve
peak
decline
baseline
Pt1
Pt4
Pt7
Pt8
Pt9
Pt11
Pt12
Pt13

Fig. S1 Immune cell chimerism analysis in post-Tx samples. (A) Representative gating strategy for T/B cell/monocyte chimerism in post-Tx BAL (Pt1 POD107). Recipient cells were identified by HLA-A3+ HLA-ABC+ expression. Donor cells were identified by HLA-A3- HLA-ABC+ expression. (B) Recipient-derived CD3+ T cells and CD14+ monocytes in BAL samples across all patients (POD7–352). (C) Longitudinal chimerism patterns showing donor T cell percentages in PBMC (left panel) and recipient T cell percentages in BAL (right panel) from Pt1 to Pt13. Black-outlines symbols indicate timepoints with pathology-determined ACR. Wilcoxon test was performed for panel B. ****p < 0.0001.

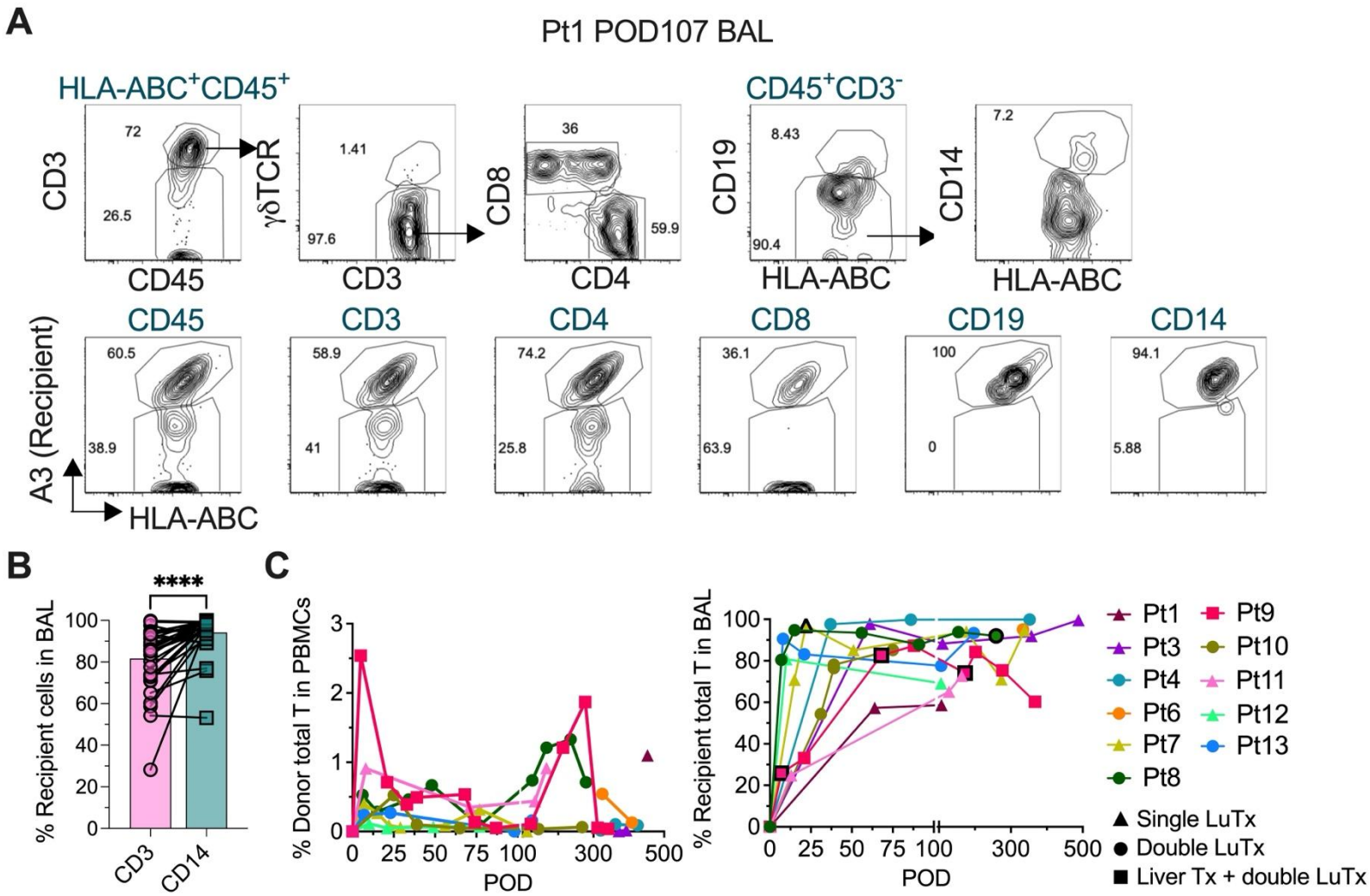

Fig. S2 Sample collection overview for TCRβ sequencing analysis. Summary of all pre-Tx and post-Tx specimens with available TCR-β sequencing data. Samples are annotated by origin (D: donor; R: recipient) and tissue types.

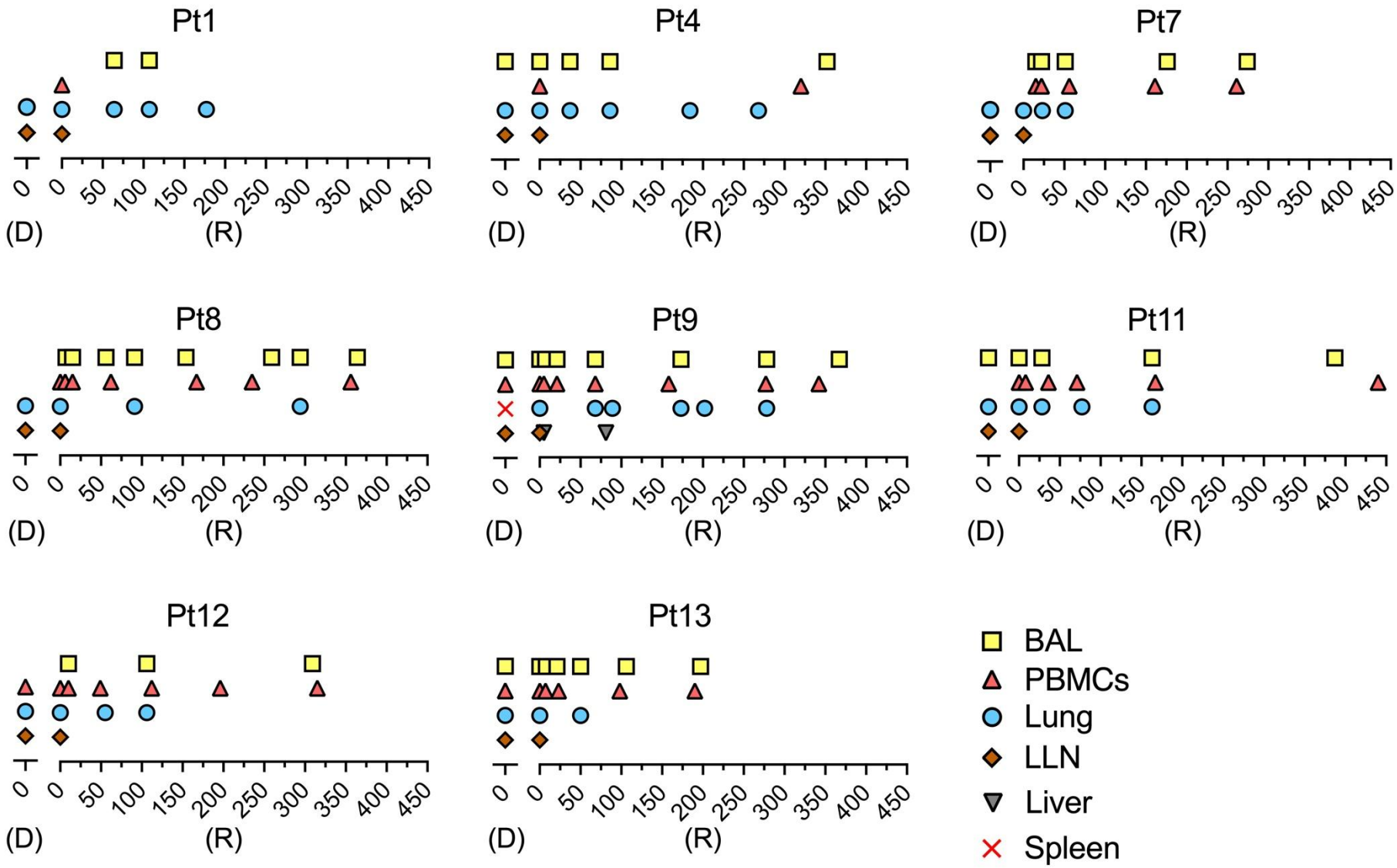

Fig. S3 TCR repertoire stability analysis using Jensen-Shannon Divergence (JSD). JSD values are plotted against the time interval (△POD, in days) between consecutive sampling time points. Correlation analyses were performed using Pearson's correlation for normally distributed data and Spearman's rank correlation for non-normally distributed data.

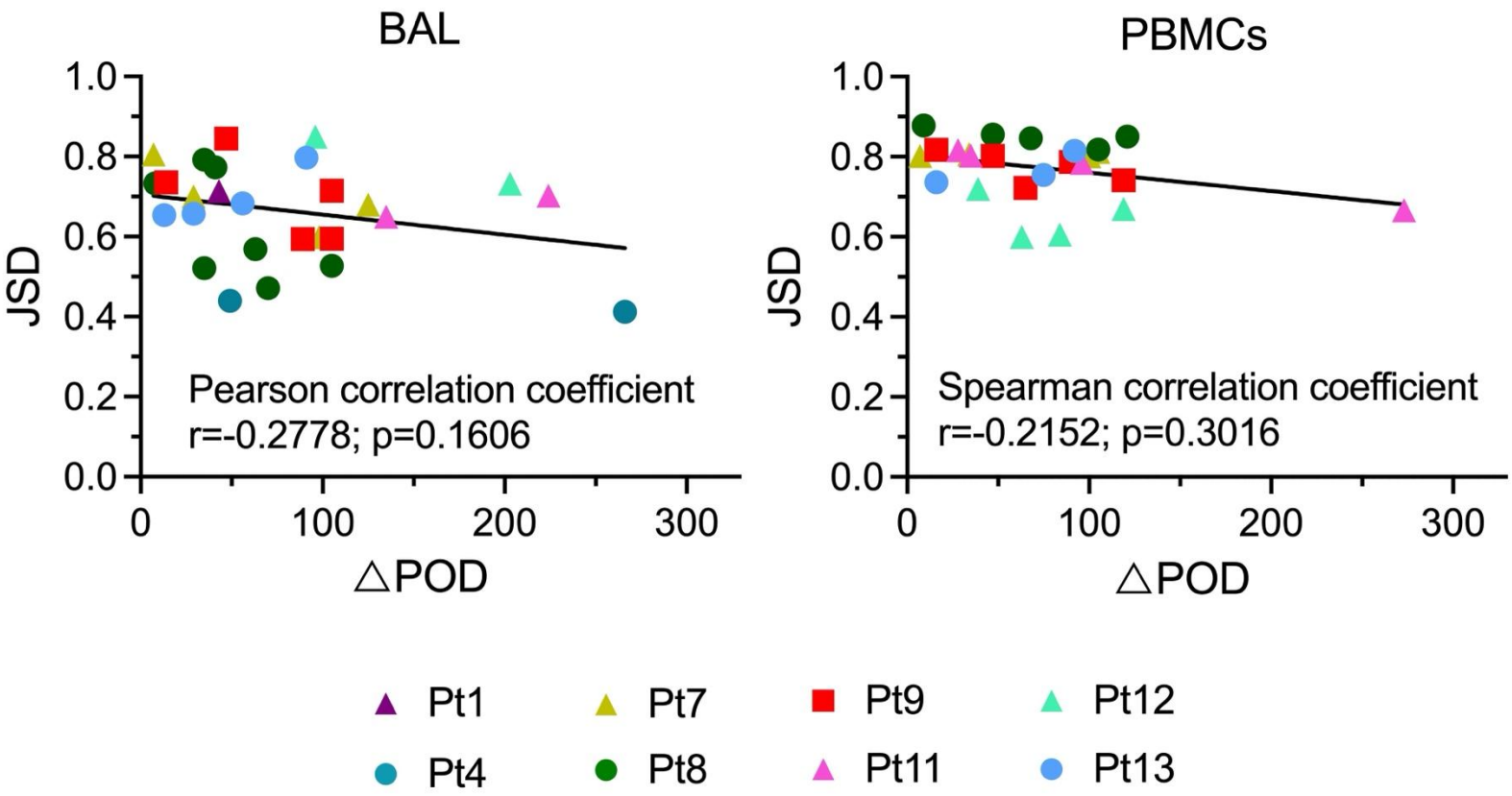

Fig. S4 Contribution of pre-existing and newly emergent TCRs to post-Tx repertoire maintenance. Pre-Tx detected recipient TCRs (A) and post-Tx newly detected TCRs (B) both contribute to TCR repertoire diversity in BAL and PBMCs. (C) Pre-Tx detected recipient TCRs (open symbols) and post-Tx newly detected TCRs (solid symbols) demonstrate distinct recurrence patterns during immune reconstitution.

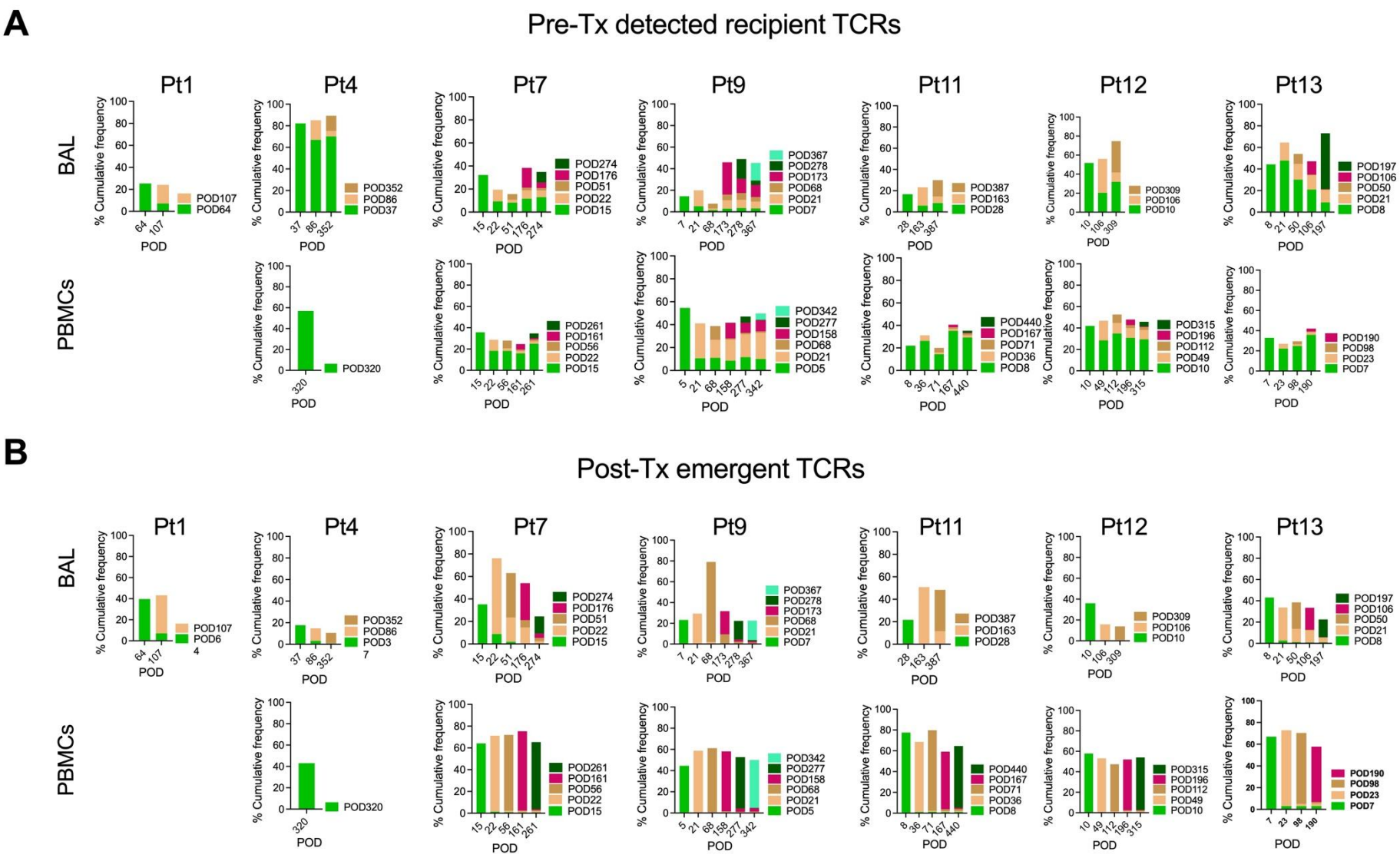

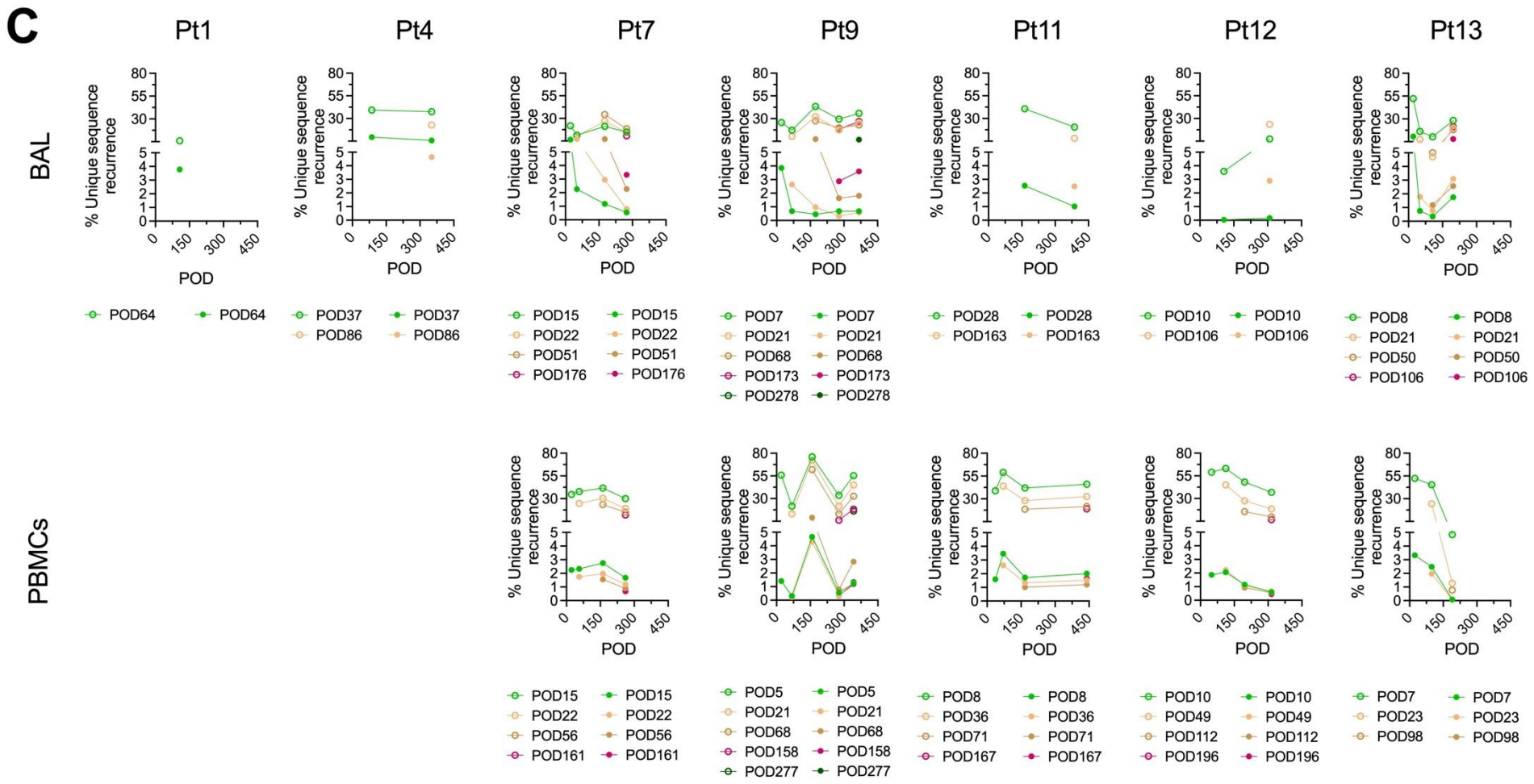
C
Pt1
Pt4
Pt7
Pt9
Pt11
Pt12
Pt13
BAL
PBMCs
% Unique sequence recurrence
POD
POD64
POD37
POD86
POD15
POD22
POD51
POD176
POD7
POD21
POD68
POD173
POD278
POD28
POD163
POD10
POD106
POD8
POD50
POD56
POD161
POD5
POD158
POD277
POD36
POD71
POD167
POD49
POD112
POD196
POD23
POD98

Fig. S5 Recurrence dynamics of pre-existing recipient TCR subsets. (A) Recurrence proportions of pre-Tx detected recipient TCRs stratified by CD4+ and CD8+ subsets in BAL and blood samples. (B) Comparison of recurrence between the earliest detected pre-Tx recipient CD4+ and CD8+ TCR subsets across patients. Recurrence values were normalized by the area under curve (AUC) divided by the observation time span (as shown in panel A). Paired t test was performed for panel B. Solid horizontal bars indicate means. *$p < 0.05$.

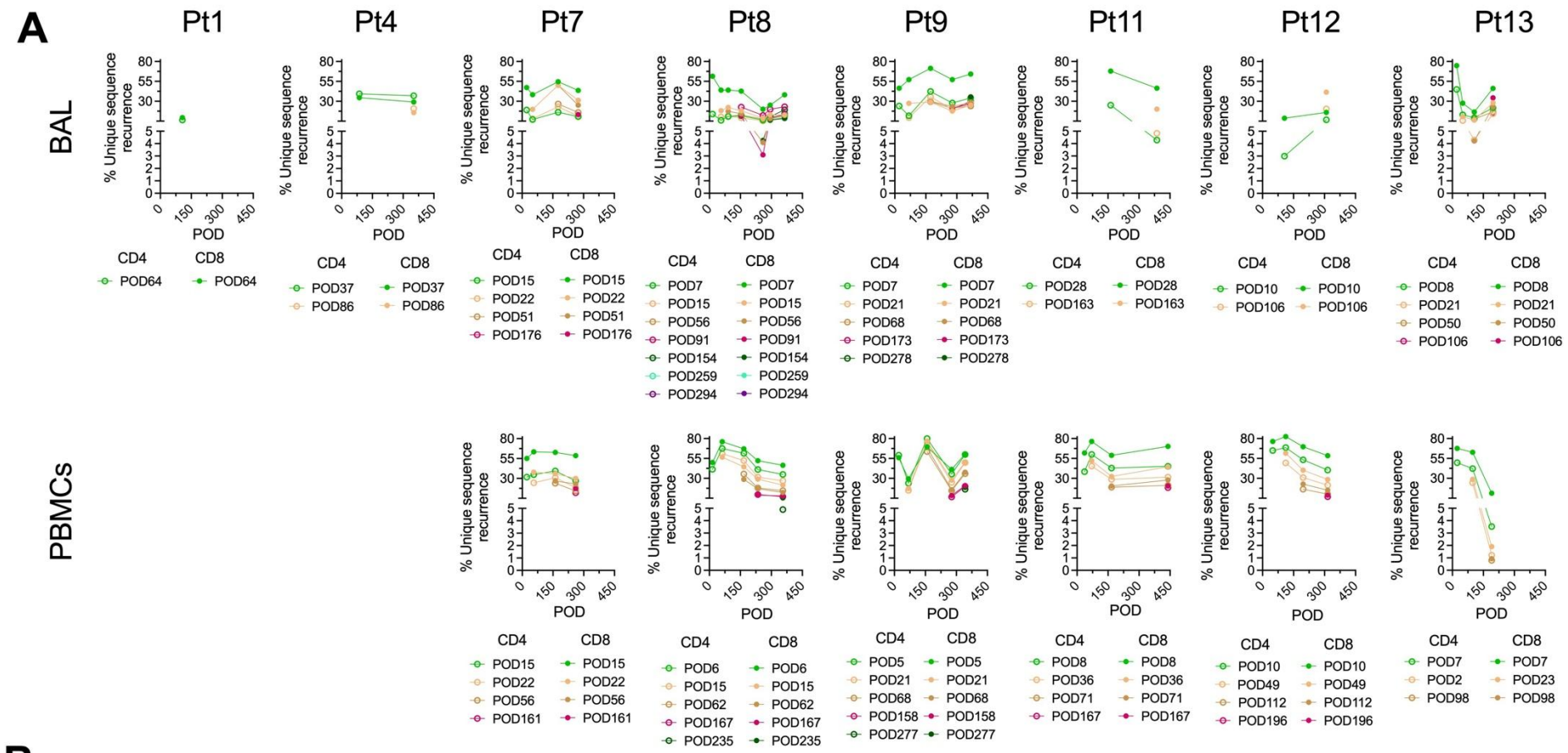
A
Pt1
Pt4
Pt7
Pt8
Pt9
Pt11
Pt12
Pt13
BAL
PBMCs
% Unique sequence recurrence
POD
CD4
CD8
POD64
POD37
POD86
POD15
POD22
POD51
POD176
POD7
POD56
POD91
POD154
POD259
POD294
POD21
POD68
POD173
POD278
POD28
POD163
POD10
POD106
POD8
POD50
POD161
POD6
POD62
POD167
POD235
POD5
POD158
POD277
POD36
POD71
POD49
POD112
POD196
POD2
POD23
POD98

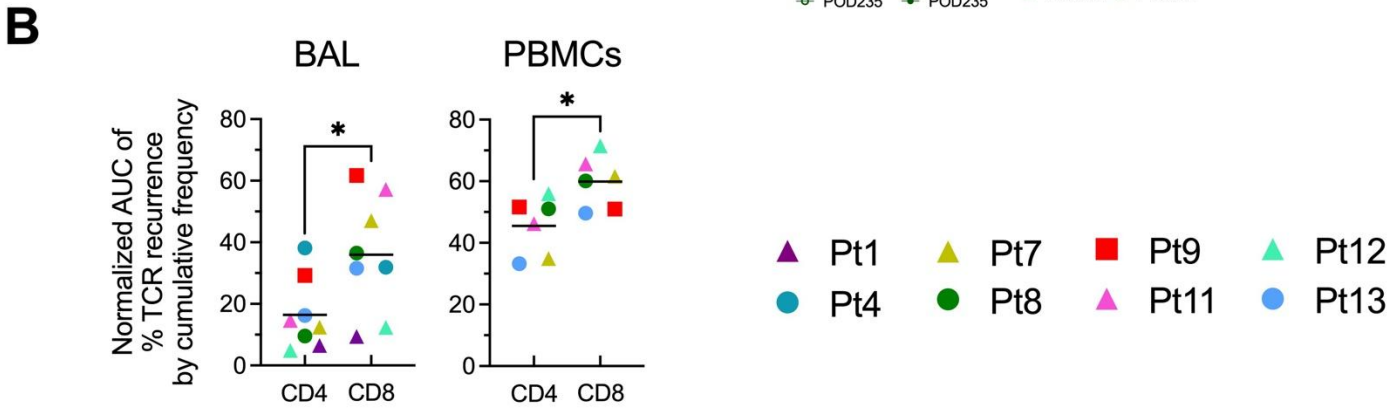
B
BAL
PBMCs
Normalized AUC of % TCR recurrence by cumulative frequency
CD4
CD8
*
Pt1
Pt4
Pt7
Pt8
Pt9
Pt11
Pt12
Pt13

Fig. S6 Composition of T cell subsets by tissue origin. Cumulative frequencies of recipient TCRs classified as “lymphoid-PBMC-lung shared”, “lymphoid-lung shared”, “PBMC-lung shared”, “lymphoid-PBMC shared”, “lymphoid only”, “PBMC only”, and “lung only” in pre-Tx and post-Tx samples. R4U: recipient CD4 unstimulated; R8U: recipient CD8 unstimulated; R4L: recipient CD4 CFSE^{low}; R8L: recipient CD8 CFSE^{low}.

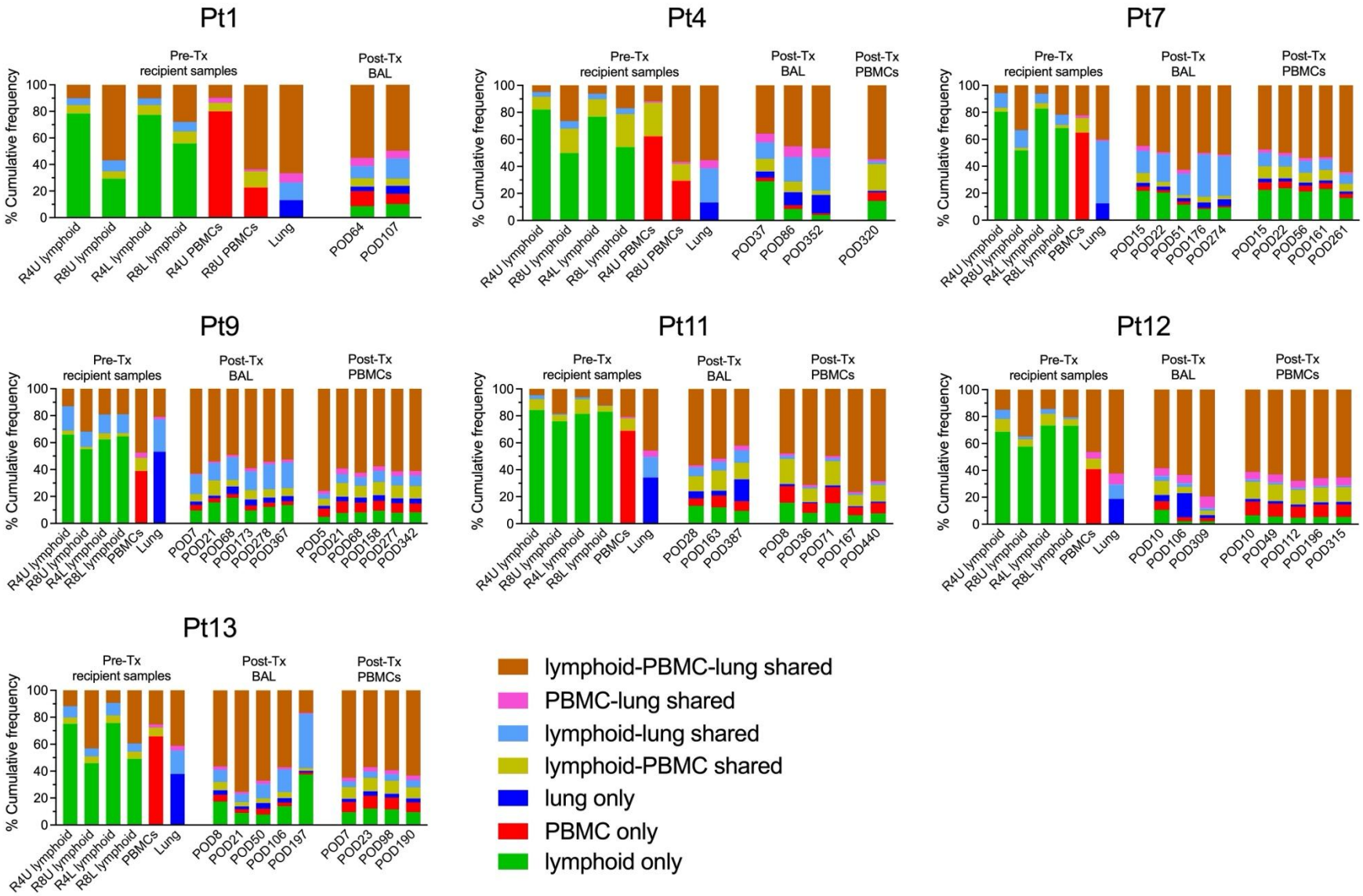

Fig. S7 Characterization of COVID-19-reactive TCRs by alloreactivity status. (A) Composition of COVID-19-specific TCRs in Pt13 at the unique sequence level subgrouped by alloreactive vs nonalloreactive identification in pre-Tx MLRs, including CD4 and CD8 GvH and nonGvH, HvG and nonHvG categories. Pie chart centers indicate total unique TCRs reactive to COVID-19 in all samples sequenced from Pt13. (B) Cumulative frequency of COVID-19-specific TCRs in post-Tx samples (n=8 patients), stratified by alloreactive (CD4 HvG, CD8 HvG, CD4 GvH, CD8 GvH) vs nonalloractive (CD4 nonHvG, CD8 nonHvG, CD4 nonGvH, CD8 nonGvH) identification. Wilcoxon tests were performed for panel B. Dotted horizontal bars indicate medians. *p < 0.05, **p < 0.01, ***p < 0.001, ****p < 0.0001.)

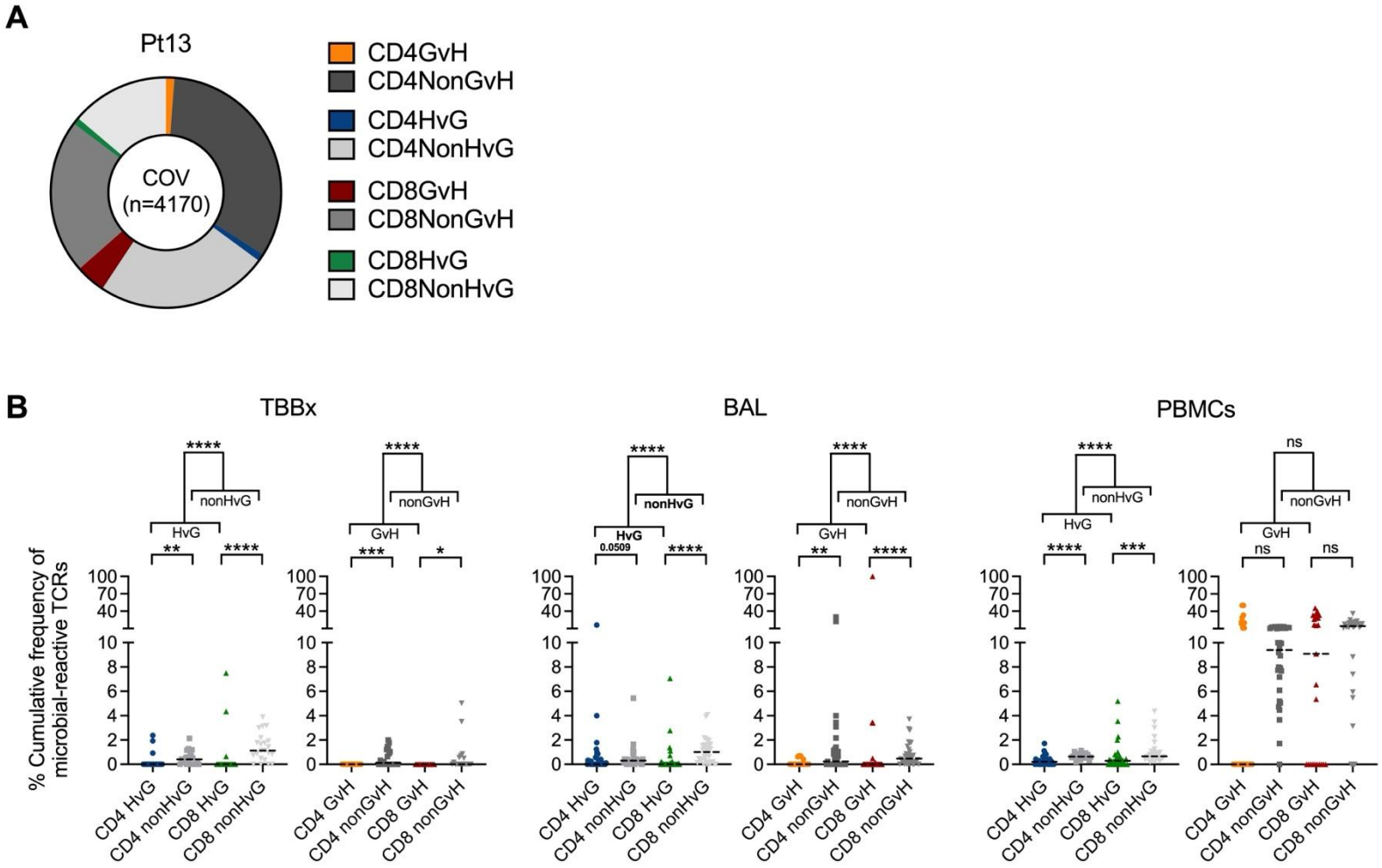

Fig. S8 Tracking of alloreactive clones and pulmonary function post-Tx. (A) Cumulative frequency of GvH and HvG clones in BAL specimens in Pts8, 11, 12, and 13. (B) Percentage cumulative frequency of HvG-reactive sequences among recipient mappable repertoires in post-Tx PBMC, BAL and lung allografts in rPts8, 11, 12, and 13. (C) Left Y axis: The FEV1/baseline FEV1 proportion cross time curve of all the patients. Right Y axis: Percentage cumulative frequency of HvG-reactive sequences among recipient mappable repertoires in post-Tx BAL labeled with peak, decline and baseline phases. Some peak phases were defined as a range rather than a single peak value for HvG clones in BAL, due to the lack of FEV1/baseline data corresponding to the peak HvG values. Additionally, the earliest HvG mesurements in BAL were excluded from the correlation analysis in Fig. 5D because of missing adjacent FEV1/baseline data. FEV1: forced expiratory volume in one second.

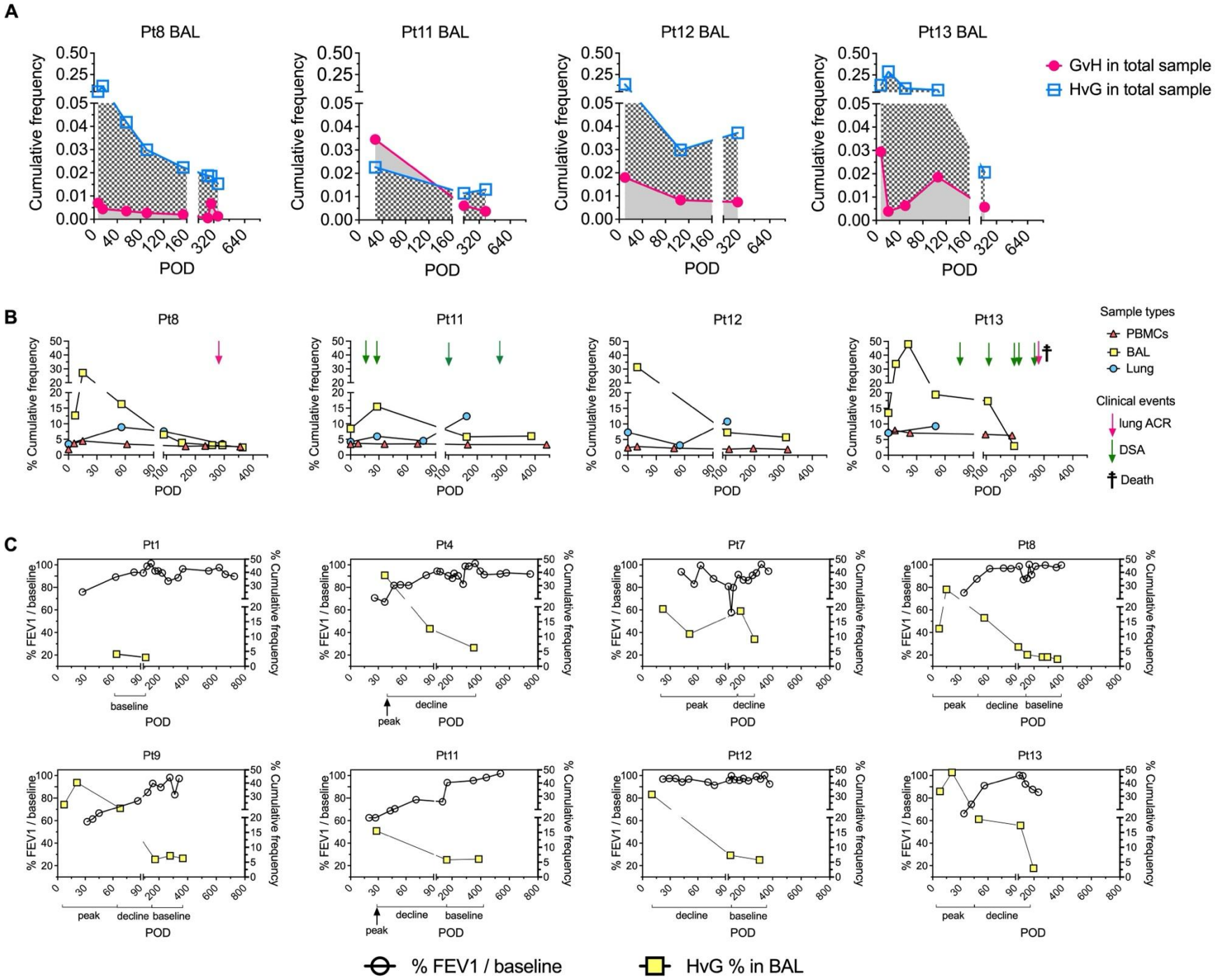
A
Pt8 BAL
Pt11 BAL
Pt12 BAL
Pt13 BAL
Cumulative frequency
POD
GvH in total sample
HvG in total sample
B
Pt8
Pt11
Pt12
Pt13
% Cumulative frequency
POD
Sample types
PBMCs
BAL
Lung
Clinical events
lung ACR
DSA
Death
C
Pt1
Pt4
Pt7
Pt8
Pt9
Pt11
Pt12
Pt13
% FEV1 / baseline
% Cumulative frequency
POD
baseline
peak
decline
% FEV1 / baseline
HvG % in BAL

Table S1. Epidemiological and clinical characteristics of patients. F: female. M: male. COVID-19: coronavirus disease 2019. CMV: Cytomegalovirus. BKV: BK polyomavirus. EBV: Epstein-Barr virus. HBV: Hepatitis B virus. HCV: Hepatitis C virus. VZV: Varicella zoster virus. Precise ages were replaced with age ranges as required.

Pt #	Recipient Age at Tx (yrs)	Recipient Sex	Indication for Transplant	Type of LuTx	Donor Age (yrs)	Donor Sex	Infection	Rejection	CLAD	Death (Cause of death)
1	61-65	F	Pulmonary emphysema	Single	46-50	M	Kiebsiella /COVID-19 /CMV	No	No	No
2	71-75	M	Chronic atrial fibrillation	Single	46-50	M	No	No	No	Yes (POD166: cardiopulmonary arrest secondary to complications related to hypoxia and atrial fibrillation and rapid ventricular response)
3	66-70	M	Interstitial lung disease	Single	11-15	M	Stenotrophomonas maltophilia / Lomentospora	POD327: A0B1R	Yes	Yes (POD1427: respiratory failure. Contributory causes: gastrointestinal hemorrhage and skin malignancy).
4	61-65	F	Interstitial lung disease, pulmonary hypertension	Double	16-20	F	aspergillus / pseudomonas aeruginosa / klebsiella / mycobacterium avium / CMV / BKV	POD924: minimal ACR (A1B0)	Yes	Yes (POD1556: respiratory failure. Contributory cause: liver failure).

5	61-65	F	Pulmonary hypertension	Double	61-65	M	No	No	No	Yes (POD16: bowel perforation with multisystem organ failure)
6	66-70	M	Pulmonary hypertension	Double	21-25	M	Stenotrophomonas maltophilia / CMV	No	No	No
7	66-70	M	Interstitial lung disease, chronic obstructive pulmonary disease, idiopathic pulmonary fibrosis, bronchiolitis obliterans with organizing pneumonia	Single	51-55	F	aspergillus	POD23: mild ACR (A2B0)	No	No
8	51-55	F	Idiopathic pulmonary fibrosis, Sjogren's related nonspecific interstitial pneumonitis, severe pulmonary hypertension	Double	31-35	F	CMV / pluralibacter	POD259: minima l ACR (A1B0)	No	No
9	26-30	M	Cystic fibrosis	Double lung + Liver	31-35	F	scedosporium apiospermum / enterobacter cloacae / staph aureus / EBV	POD4: mild-moderate ACR in liver; POD67: mild ACR in lung (A2B1R); POD69: mild ACR in liver; POD80: minimal ACR in liver; POD172: minimal ACR in lung (A1BX)	No	No

10	41-45	F	Pulmonary hypertension	Double lung	36-40	F	Candida tropicalis / rhino / enterovirus / CMV	No	No	No
11	31-35	M	Interstitial lung disease related to connective tissue disease, systemic sclerosis	Single Right	31-35	M	staph aureus / CMV / E. coli / rhizopus spp / coronavirus HKU1	No	No	No
12	61-65	F	Interstitial lung disease, idiopathic pulmonary fibrosis	Single Right	46-50	F	HBV / HCV / penicillium / parainfluenza virus 1 / actinomyces	No	No	No
13	31-35	M	Pulmonary sarcoidosis	Double	11-15	M	CMV / EBV / VZV / measles / rubella / candida / TB / pseudomonas aeruginosa / mycobacterium / parainfluenza	POD279: mild ACR (A2BX)	No	Yes (POD303: multisystem organ failure)

Table S2. HLA-A, B typing and anti-HLA allotype antibodies used to distinguish donor from recipient cells in lung transplant recipients. HLA-A09 is a broad antigen HLA-A serotype that recognized the HLA-A23 and HLA-A24 serotypes. HLA-A28 is a broad antigen HLA-A serotype that recognized the HLA-A68 and HLA-A69 serotypes. HLA-B12 is a broad antigen HLA-B serotype that recognized the HLA-B44 and HLA-B45 serotypes.

Pt#	Recipient HLA-A, B type	Donor HLA-A, B type	HLA allotype-specific antibodies used to distinguish between recipient and donor cells
1	**A03** / A29	A30 / A36	Anti-HLA A3 APC
	B27 / B44	B42 / B53	
2	**A03** / A29	A30 / A36	Anti-HLA A3 APC, Anti-HLA B12 FITC
	B61 / **B44**	B42 / B53	
3	**A02** / A03	A01 / A03	Anti-HLA A2/A28 biotin, Anti-HLA B8 FITC
	B39 / B44	**B08** / B35	
4	**A03** / A31	A24 / **A68**	Anti-HLA A3 APC, Anti-HLA A2/A28 biotin
	B35 / B58	B71 / B35	
5	A02 / **A03**	A02 / A29	Anti-HLA A3 APC, Anti-HLA B12 FITC
	B35 / B61	B35 / **B44**	
6	A34 / A74	**A02** / A24	Anti-HLA A2/A28 biotin
	B72 / B53	B35 / B61	
7	A02 / A32	A02 / **A03**	Anti-HLA B12 FITC, Anti-HLA A3 APC
	B44 / B52	B13 / B51	
8	A33 / **A68**	A31 / A32	Anti-HLA A2/A28 biotin
	B07 / B53	B35 / B51	
9	**A02** / **A24**	A30 / A74	Anti-HLA A2 FITC, Anti-HLA A09 biotin
	B35 / B45	B72 / B42	
10	A01 / A25	A01 / A31	Anti-HLA B7 APC
	B08 / B18	**B07** / B08	
11	A01 / **A68**	A33 / A66	Anti-HLA A2/A28 biotin
	B35 / B61	B65 / B53	
12	A02 / A30	A02 / A11	Anti-HLA B12 FITC

	B71 / B53	B35 / **B44**	
13	A02 / **A24**	A02 / A33	Anti-HLA A9 FITC, Anti-HLA Bw4 biotin
	B60 / B57	B39 / B65	
	Bw4 / Bw6	Bw6 / Bw6	

Table S3. List of flow cytometric antibodies used in the study.

Antibody	Source	Identifier
Mouse anti-Human CD3 (clone SP34-2) PerCP-Cy5.5	BD Biosciences	Cat#552852; RRID: AB_394493
Mouse anti-Human CD4 (clone OKT4) AF700	Tonbo	Cat#80-0048; RRID: AB_2621976
Mouse anti-Human CD8 (clone SK1) APC-Cy7	BD Biosciences	Cat#561945; RRID: AB_396892
Mouse anti-Human CD8 (clone SK1) Biotin	BioLegend	Cat#344720; RRID: AB_2828353
Mouse anti-Human CD14 (clone M5E2) FITC	BioLegend	Cat#982502; RRID: AB_2616906
Mouse anti-Human CD14 (clone M5E2) APC-Cy7	BioLegend	Cat#301820; RRID: N/A
Mouse anti-Human CD19 (clone SJ25C1) BUV496	BD Biosciences	Cat#612938; RRID: AB_2870221
Mouse anti-Human CD28 (clone CD28.2) Pacific Blue	BioLegend	Cat#302928; RRID: AB_10641279
Mouse anti-Human CD31 (clone WM-59) BV605	BD Biosciences	Cat#562855; RRID: AB_2737841
Mouse anti-Human CD45 (clone HI30) PE-CF594	BD Biosciences	Cat#562279; RRID: AB_11154577
Mouse anti-Human CD45RA (clone HI100) Brilliant Violet 510	BioLegend	Cat#304142; RRID: AB_2561947
Mouse anti-Human CD49a (clone SR84) BUV395	BD Biosciences	Cat#742363; RRID: AB_2740721
Mouse anti-Human CD56 (clone HCD56) Brilliant Violet 605	BioLegend	Cat#318334; RRID: AB_2561912
Mouse anti-Human CD69 (clone FN50) Brilliant Violet 650	BioLegend	Cat#310934; RRID: AB_256315
Mouse anti-Human CD103 (clone Ber-ACT8) Brilliant Violet 711	BioLegend	Cat#350222; RRID: AB_2629651
Mouse anti-Human CD197 (CCR7) (clone G043H7) PE	BioLegend	Cat#353204; RRID: AB_10913813
Mouse anti-Human CD314 (NKG2D) (clone 1D11) APC	BioLegend	Cat#320808; RRID: AB_492962
Mouse anti-Human HLA-A2/A28 (clone N/A) Biotin	One Lambda	Cat#BIH0037; RRID: N/A
Mouse anti-Human HLA-A2/A28 (clone REA142) FITC	Miltenyi Biotech	Cat#130-099-601; RRID: AB_2652040
Mouse anti-Human HLA-A2 (clone BB7.2) FITC	BioLegend	Cat#343304; RRID: AB_1659245
Mouse anti-Human HLA-A3 (clone GAP.A3) APC	Thermo Fisher Scientific	Cat#17-5754-42; RRID: AB_2573220
Mouse anti-Human HLA-A9 (clone N/A) Biotin	One Lambda	Cat#BIH0964; RRID: N/A
Mouse anti-Human HLA-A9 FITC (clone N/A)	One Lambda	Cat#FH0964; RRID: N/A
Mouse anti-Human HLA-A29 (clone N/A) Biotin	One Lambda	Cat#BIH0155; RRID: N/A
Mouse anti-Human HLA-ABC (clone G56-2.6) APC	BD Biosciences	Cat#555555; RRID: AB_398603
Mouse anti-Human HLA-ABC (clone G46-2.6) BV786	BD Biosciences	Cat#740982; RRID: AB_2740606
Mouse anti-Human HLA-B8 (clone N/A) FITC	One Lambda	Cat#FH0536A; RRID: N/A
Mouse anti-Human HLA-B12 (clone REA138) FITC	Miltenyi Biotech	Cat#130-099-860; RRID: AB_2652098
Mouse anti-Human HLA-Bw4 (clone REA274) Biotin	Miltenyi Biotech	Cat#130-123-859; RRID: AB_2889687
Mouse anti-Human HLA-Bw6 (clone REA143) APC	Miltenyi Biotech	Cat#130-099-845; RRID: AB_2652026

Streptavidin Alexa Fluor 594	Thermo Fisher Scientific	Cat#S32356; RRID: N/A
Streptavidin BUV737	BD Biosciences	Cat#564293; RRID: AB_2869560
Mouse anti-Human gdTCR (clone IMMU510) PE-Cy7	Beckman Coulter	Cat#B10247; RRID: N/A

Table S4. Unique sequence counts and total template counts of TCRs identified in pre-Tx tissues. Unique sequence counts of pre-Tx detected single- or multi-tissue distributed TCRs. LLN: lung-associated lymph nodes. PBMC: peripheral blood mononuclear cells. U: unstimulated. L: $CFSE^{low}$.

Patient ID	Recipient pre-Tx tissues	Unique sequence counts	Total template counts	Lymphoid only unique sequence counts	Lung only unique sequence counts	PBMC only unique sequence counts	Lymphoid-lung shared unique sequence counts	Lymphoid-PBMC shared unique sequence counts	PBMC-lung shared unique sequence counts	Lymphoid-PBMC-lung shared unique sequence counts
Pt1	LLN_CD4_U	67920	88518	80724	8825	68379	3078	4771	1839	3257
	LLN_CD8_U	21333	104728							
	LLN_CD4_L	2516	20565							
	LLN_CD8_L	661	12287							
	Lung	17015	139407							
	PBMC_CD4	72338	90842							
	PBMC_CD8	5980	19652							
Pt4	LLN_CD4_U	214100	379958	224935	4062	55144	3860	13238	630	3120
	LLN_CD8_U	22825	49985							
	LLN_CD4_L	7754	191220							
	LLN_CD8_L	3895	162298							
	Lung	11688	49298							
	PBMC_CD4	49616	63361							
	PBMC_CD8	22693	72016							
Pt7	LLN_CD4_U	290715	448551	306266	14279	36938	12238	5005	729	3141
	LLN_CD8_U	23741	52735							
	LLN_CD4_L	13680	237954							
	LLN_CD8_L	2941	167535							
	Lung	30406	224480							
	PBMC	45851	61169							
Pt8	LLN_CD4_U	234517	289102	312474	8752	56719	5069	4365	304	1071
	LLN_CD8_U	80256	191459							

	LLN_CD4_L	8383	223318							
	LLN_CD8_L	1079	33483							
	Lung	15242	34072							
	PBMC	62581	76722							
Pt9	LLN_CD4_U	171022	238144	222683	34664	92761	5443	24500	2428	8980
	LLN_CD8_U	58911	107118							
	LLN_CD4_L	28464	350441							
	LLN_CD8_L	12305	334080							
	Lung	128933	196808							
	PBMC	51624	99372							
Pt11	LLN_CD4_U	275730	336802	377924	21285	210989	5385	17603	2187	5684
	LLN_CD8_U	118868	169625							
	LLN_CD4_L	6390	181288							
	LLN_CD8_L	7570	400189							
	Lung	34585	75603							
	PBMC	236774	329788							
Pt12	LLN_CD4_U	211106	288940	231397	41432	189385	10367	18273	9151	15096
	LLN_CD8_U	48127	76820							
	LLN_CD4_L	13913	335910							
	LLN_CD8_L	5993	353851							
	Lung	76226	314278							
	PBMC	232389	555188							
Pt13	LLN_CD4_U	150305	206898	183227	33630	117539	9659	7597	2428	6460
	LLN_CD8_U	39383	82262							
	LLN_CD4_L	17324	330970							
	LLN_CD8_L	5613	279729							
	Lung	52273	99088							
	PBMC	134314	213642							

Table S5. Absolute number and cumulative frequency of GvH and HvG CD4 and CD8 clones identified by TCRβ CDR3 DNA sequencing in pre-Tx LLN and post-Tx BAL, PBMC and TBBx in LuTx patients. “Cumulative frequency (Cum.freq.)” was calculated as a percentage of all sequences weighted by copy numbers in designated populations. LLN: lung-associated lymph nodes. BAL: bronchoalveolar lavage. TBBx: transbronchial biopsies. U: unstimulated. L: CFSE^{low}. GvH: graft-versus-host. HvG: host-versus-graft.

			Mappable clones				Mappable alloreactive clones				Cumulative frequency of alloreactive clones				Total	
Patient #	T cell source	POD	D CD4	D CD8	R CD4	R CD8	GvH CD4	GvH CD8	HvG CD4	HvG CD8	GvH CD4	GvH CD8	HvG CD4	HvG CD8	Cum. freq. of GvH	Cum. freq. of HvG
Pt1	LLN	0 (L+U)					3813	1692	2473	569						
	LLN	0 (U)	87273	66061	67920	21333	491	213	268	194	0.7474	1.0227	0.7569	3.4079		
	BAL	64	200	271	306	198	22	7	16	6	0.7486	0.3622	0.6762	0.1449	1.1108	0.8211
	BAL	107	49	87	98	44	5	6	4	1	0.8037	1.1481	0.4592	0.1148	1.9518	0.5741
	TBBx	64	89	234	190	199	5	7	13	11	0.2218	0.7542	0.6211	0.8873	0.9760	1.5084
	TBBx	107	84	199	147	156	8	8	0	8	0.5291	1.1243	0	0.5952	1.6534	0.5952
	TBBx	177	139	214	202	202	13	5	11	14	0.7788	0.5711	0.6231	1.0384	1.3499	1.6615
Pt4	LLN	0 (L+U)					4895	2286	4156	1909						
	LLN	0 (U)	332697	25963	214100	22825	856	347	1227	345	0.7828	2.3224	1.1414	2.5288		
	PBMC	320	50	10	6221	2551	0	0	109	128	0	0	0.4919	0.5530	0	1.0449
	BAL	37	86	11	8781	3051	0	0	208	130	0	0	10.2361	16.5146	0	26.7508
	BAL	86	5	4	1693	638	0	1	98	86	0	0.0113	4.1070	4.4116	0.0113	8.5186
	BAL	352	5	4	1469	451	0	1	66	61	0	0.0047	3.3055	1.0623	0.0047	4.3678
	TBBx	37	4	1	1589	487	0	0	35	25	0	0	4.1667	5.8532	0	10.0198
	TBBx	86	40	9	6701	2311	0	0	18	9	0	0	1.7857	1.8849	0	3.6706
	TBBx	184	0	5	330	135	0	0	22	39	0	0	2.9795	5.4004	0	8.3799
	TBBx	268	1	0	170	73	0	0	19	19	0	0	1.7059	2.1121	0	3.8180
Pt7	LLN	0 (L+U)					2759	416	6298	1661						
	LLN	0 (U)	186276	14448	290715	23741	523	146	1262	231	0.2808	1.0105	0.4341	0.9730		
	PBMC	15	77	16	6717	985	1	1	227	51	0.0018	0.0018	0.5659	0.3539	0.0036	0.9199

	PBMC	22	54	7	7835	1000	1	0	246	64	0.0012	0	0.5452	0.2522	0.0012	0.7974
	PBMC	56	64	8	8919	1278	2	3	271	79	0.0019	0.0253	0.4131	0.2904	0.0272	0.7034
	PBMC	161	95	11	11433	1293	1	0	272	63	0.0006	0	0.2929	0.1992	0.0006	0.4922
	PBMC	261	46	7	6942	1132	0	0	200	73	0	0	0.3814	0.4640	0	0.8454
	BAL	15	153	109	515	110	19	12	69	12	0.5618	1.1827	3.2229	0.6209	1.7445	3.8439
	BAL	22	77	85	737	228	3	7	135	27	0.0304	0.1139	2.9546	0.5772	0.1443	3.5318
	BAL	51	25	114	225	141	1	10	43	17	0.0175	0.6132	1.0161	0.5606	0.6307	1.5767
	BAL	176	27	133	1066	422	1	9	137	35	0.0066	0.2171	5.5318	1.1774	0.2236	6.7092
	BAL	274	26	132	492	203	1	9	58	20	0.0219	0.8321	2.2115	0.7445	0.8540	2.9560
	TBBx	23	74	63	446	128	6	6	54	6	0.1691	0.1972	1.9724	0.1972	0.3663	2.1696
	TBBx	51	43	38	416	153	3	4	57	13	0.1427	0.3330	3.1399	0.6185	0.4757	3.7583
Pt8	LLN	0 (L+U)					6120	2835	4409	1008						
	LLN	0 (U)	189767	140867	234517	80256	747	349	499	143	0.3936	0.2478	0.2128	0.1782		
	PBMC	6	72	88	3024	951	2	3	102	21	0.0034	0.0101	0.1653	0.6298	0.0135	0.7951
	PBMC	15	149	88	6125	1622	9	5	162	22	0.0064	0.0042	0.2413	0.3815	0.0106	0.6228
	PBMC	62	460	280	16463	4562	13	9	393	54	0.0027	0.0020	0.2250	0.4390	0.0047	0.6640
	PBMC	167	366	254	13573	3167	13	6	236	36	0.0038	0.0013	0.1074	0.3228	0.0052	0.4302
	PBMC	235	147	107	6988	1893	4	3	139	23	0.0035	0.0021	0.1584	0.3910	0.0057	0.5494
	PBMC	356	75	52	5473	1461	1	3	99	25	0.0011	0.0033	0.1849	0.3358	0.0044	0.5207
	BAL	7	135	120	446	236	17	4	46	10	0.5533	0.1456	1.6308	3.4362	0.6989	5.0670
	BAL	15	78	137	646	343	9	11	232	15	0.1225	0.3184	6.2217	5.4991	0.4409	11.7208
	BAL	56	65	153	415	238	3	10	67	9	0.0618	0.2885	2.1430	2.0400	0.3503	4.1830
	BAL	91	75	172	581	262	3	6	56	11	0.0583	0.2138	1.6910	1.3022	0.2721	2.9932
	BAL	154	66	168	614	256	5	5	35	13	0.1153	0.0865	1.3118	0.9226	0.2018	2.2344
	BAL	259	27	59	319	126	0	1	13	5	0.0000	0.0494	1.4829	0.3955	0.0494	1.8784
	BAL	294	63	120	465	159	2	0	23	8	0.6695	0.0000	1.3694	0.4869	0.6695	1.8564
	BAL	364	50	178	860	247	1	4	26	7	0.0141	0.1124	1.1945	0.3373	0.1265	1.5318
	TBBx	91	84	47	91	74	3	2	6	5	0.4994	0.2497	0.9988	1.1236	0.7491	2.1223
	TBBx	294	78	47	73	36	3	0	3	1	0.9107	0.0000	0.5464	0.3643	0.9107	0.9107
Pt9	LLN	0 (L+U)					9201	7222	8415	5170						
	LLN	0 (U)	196528	122773	171022	58911	1619	729	1329	523	1.6800	2.5951	1.3979	1.9194		
	PBMC	5	14	11	599	102	2	2	41	8	0.0784	0.0523	1.2807	0.2352	0.1307	1.5159
	PBMC	21	67	48	6687	1069	5	4	341	54	0.0079	0.0095	1.4133	0.1577	0.0174	1.5710

	PBMC	68	2	10	1879	349	0	0	80	15	0	0	0.9768	0.1431	0	1.1199
	PBMC	158	267	180	18486	3461	12	22	751	206	0.0067	0.0096	1.3029	0.1900	0.0163	1.4928
	PBMC	277	18	12	3270	661	0	1	170	33	0	0.0055	1.6751	0.2425	0.0055	1.9176
	PBMC	342	48	40	8126	1541	0	3	374	84	0	0.0047	1.5835	0.2396	0.0047	1.8231
	BAL	7	516	267	187	28	100	34	46	6	7.1429	3.6680	2.6544	0.4826	10.8108	3.1371
	BAL	21	1990	741	1032	137	296	89	260	31	6.7296	3.0816	7.0091	0.3852	9.8112	7.3943
	BAL	68	285	472	538	254	55	75	115	40	0.6051	2.3869	1.1248	0.3007	2.9919	1.4254
	BAL	173	277	498	3024	461	44	72	203	31	1.0671	3.6108	2.0073	0.4153	4.6779	2.4226
	BAL	278	134	340	1689	312	31	46	118	34	0.9971	1.9326	1.9120	1.2747	2.9297	3.1867
	BAL	367	187	437	2971	610	38	54	197	48	1.8800	1.2054	1.9439	0.6506	3.0855	2.5945
	TBBx	68	56	45	226	80	6	6	36	9	0.4205	0.5606	2.8732	0.7008	0.9811	3.5739
	TBBx	89	10	9	175	69	0	0	18	4	0	0	2.4862	0.5525	0.0000	3.0387
	TBBx	173	2	1	195	41	1	0	15	3	0.1969	0	3.1496	0.5906	0.1969	3.7402
	TBBx	202	86	78	1116	197	8	12	86	17	0.3161	0.4109	3.1922	0.7269	0.7269	3.9191
	TBBx	278	7	31	976	292	1	4	64	24	0.0289	0.2888	2.4256	1.1551	0.3176	3.5807
	liver Bx	5	316	181	931	158	54	14	138	27	1.8260	0.7101	4.8948	1.7246	2.5361	6.6193
	liver Bx	81	3	5	468	347	0	1	67	33	0	0.0245	2.4205	1.1002	0.0245	3.5208
Pt11	LLN	0 (L+U)					2883	1815	3817	4280						
	LLN	0 (U)	222042	46584	275730	118868	682	133	611	253	0.5820	1.6785	0.4792	0.9155		
	PBMC	8	441	175	16284	4025	6	8	359	160	0.0022	0.0034	0.2654	0.4217	0.0056	0.6872
	PBMC	36	372	177	14775	4030	6	9	305	152	0.0027	0.0150	0.1852	0.8093	0.0177	0.9945
	PBMC	71	753	276	28149	6041	12	13	468	224	0.0016	0.0050	0.2018	0.4039	0.0066	0.6057
	PBMC	167	320	127	16685	3910	7	9	324	143	0.0019	0.0118	0.2219	1.0237	0.0137	1.2456
	PBMC	440	344	123	18004	4956	4	10	346	163	0.0010	0.0021	0.2525	0.7865	0.0030	1.0390
	BAL	28	294	269	140	112	16	23	26	11	0.6587	2.7917	1.5997	0.6587	3.4504	2.2585
	BAL	163	552	454	1443	673	16	22	74	44	0.1154	0.4916	0.4565	0.6872	0.6069	1.1437
	BAL	387	146	204	421	391	1	9	18	20	0.0148	0.3562	0.2968	1.0092	0.3710	1.3060
	TBBx	28	233	202	34	36	7	12	2	4	0.6426	1.4458	0.1606	0.3213	2.0884	0.4819
	TBBx	77	490	308	755	389	9	9	33	19	0.1286	0.3858	0.5715	0.5429	0.5144	1.1144
	TBBx	128	2	18	6	8	0	0	0	1	0	0	0	1.1111	0	1.1111
	TBBx	163	366	319	331	201	11	16	43	17	0.2526	1.0686	1.0297	0.6412	1.3212	1.6709
Pt12	LLN	0 (L+U)					5592	3472	5236	2458						
	LLN	0 (U)	217758	59664	211106	48127	1565	205	917	159	2.0143	0.9212	0.9140	0.9529		

	PBMC	10	61	25	6704	1771	1	0	234	45	0.0018	0.0000	0.8021	0.1622	0.0018	0.9643
	PBMC	49	184	93	18131	3706	4	4	454	93	0.0024	0.0016	0.6852	0.1811	0.0040	0.8662
	PBMC	112	238	91	20592	4338	2	6	487	107	0.0006	0.0020	0.6634	0.2128	0.0025	0.8762
	PBMC	196	127	41	12307	2898	0	1	312	66	0	0.0007	0.6845	0.1981	0.0007	0.8826
	PBMC	315	64	26	8288	2131	1	1	207	46	0.0011	0.0011	0.5511	0.1583	0.0023	0.7094
	BAL	10	386	181	1571	597	79	14	258	35	1.4544	0.3458	12.5305	1.0069	1.8002	13.5374
	BAL	106	65	82	140	93	6	2	20	4	0.6179	0.2060	2.5747	0.4119	0.8239	2.9866
	BAL	309	94	88	428	243	11	5	37	12	0.5367	0.2013	2.5159	1.2076	0.7380	3.7236
	TBBx	55	63	25	87	75	10	1	4	1	1.9064	0.1733	1.0399	0.1733	2.0797	1.2132
	TBBx	106	1088	304	526	318	152	8	67	34	5.2106	0.2402	1.9217	0.9424	5.4508	2.8640
Pt13	LLN	0 (L+U)					7957	8406	6115	2398						
	LLN	0 (U)	201323	56882	150305	39383	1034	181	1231	661	1.1068	0.5740	1.6955	6.6945		
	PBMC	7	399	184	15322	6535	18	28	670	670	0.0048	0.0066	0.3273	1.9549	0.0114	2.2822
	PBMC	23	431	179	15999	5988	18	31	755	596	0.0048	0.0084	0.3445	1.2695	0.0132	1.6141
	PBMC	98	279	127	13041	5409	5	20	575	573	0.0015	0.0066	0.3299	1.3404	0.0080	1.6703
	PBMC	190	10	4	805	793	0	0	38	82	0	0	0.4878	1.8069	0	2.2946
	BAL	8	628	205	1310	885	195	30	379	128	2.4486	0.4948	6.8680	6.3902	2.9434	13.2583
	BAL	21	489	234	2758	2941	156	28	624	384	0.2843	0.1055	4.8757	24.0390	0.3898	28.9146
	BAL	50	49	77	439	578	8	6	104	65	0.2280	0.4053	4.5593	4.7366	0.6332	9.2958
	BAL	106	50	141	337	392	11	19	82	52	0.4083	1.4447	4.6796	2.8266	1.8530	7.5063
	BAL	197	329	326	1517	1566	104	32	189	188	0.2686	0.3035	0.7146	1.3504	0.5720	2.0650
	TBBx	50	38	25	595	779	6	0	83	87	0.1214	0	2.2060	3.1370	0.1214	5.3430

Table S6. Summary of the unique sequence numbers of each type of microbial-reactive TCRs compiled from published databases.

Abbreviation	Full name	Number of unique TCRβ sequences compiled
CMV	Cytomegalovirus	209,511
EA	Enterobacter aerogenes	159
EBV	Epstein-Barr virus	4,979
E.Coli	Escherichia Coli	394
Flu	Influenza	8,215
HCV	Hepatitis C virus	662
HIV	Human immunodeficiency virus	3,339
KP	Klebsiella Pneumoniae	323
MTB	Mycobacterium tuberculosis	30,958
SA	Staphylococcus aureus	1,877
ST	Salmonella typhimurium	26,477
Shi	Shigella	318
SarsCoV-2	Severe acute respiratory syndrome Coronavirus 2	148, 679
YFV	Yellow fever virus	746